

Something something something physics

Steven Green
of Emmanuel College

A dissertation submitted to the University of Cambridge
for the degree of Doctor of Philosophy

Abstract

This thesis describes the optimisation of the calorimeter design for collider experiments at the future Compact Linear Collider (CLIC) and the International Linear Collider (ILC). The detector design of these experiments is built around high-granularity Particle Flow Calorimetry that, in contrast to traditional calorimetry, uses the energy measurements for charged particles from the tracking detectors. This can only be realised if calorimetric energy deposits from charged particles can be separated from those of neutral particles. This is made possible with fine granularity calorimeters and sophisticated pattern recognition software, which is provided by the PandoraPFA algorithm. This thesis presents results on Particle Flow calorimetry performance for a number of detector configurations. To obtain these results a new calibration procedure was developed and applied to the detector simulation and reconstruction to ensure optimal performance was achieved for each detector configuration considered.

This thesis also describes the development of a software compensation technique that vastly improves the intrinsic energy resolution of a Particle Flow Calorimetry detector. This technique is implemented within the PandoraPFA framework and demonstrates the gains that can be made by fully exploiting the information provided by the fine granularity calorimeters envisaged at a future linear collider.

A study of the sensitivity of the CLIC experiment to anomalous gauge couplings that effect vector boson scattering processes is presented. These anomalous couplings provide insight into possible beyond standard model physics. This study, which utilises the excellent jet energy resolution from Particle Flow Calorimetry, was performed at centre-of-mass energies of 1.4 TeV and 3 TeV with integrated lumi-

nosities of 1.5ab^{-1} and 2ab^{-1} respectively. The precision achievable at CLIC is shown to be approximately one to two orders of magnitude better than that currently offered by the LHC.

Finally, a study into various technology options for the CLIC vertex detector is described.

Declaration

This dissertation is the result of my own work, except where explicit reference is made to the work of others, and has not been submitted for another qualification to this or any other university. This dissertation does not exceed the word limit for the respective Degree Committee.

Andy Buckley

Acknowledgements

Of the many people who deserve thanks, some are particularly prominent, such as my supervisor...

Preface

This thesis describes my research on various aspects of the LHCb particle physics program, centred around the LHCb detector and LHC accelerator at CERN in Geneva.

For this example, I'll just mention Chapter ?? and Chapter 2.

Contents

1	Calorimeter Optimisation Studies	1
1.1	Calorimeter Optimisation Studies	1
1.2	Metric	2
1.2.1	Jet Energy Resolution	2
1.2.2	Jet Energy Resolution Decompositions	4
1.2.3	Single Particle Energy Resolution	4
1.3	Event Generation, Simulation and Reconstruction	5
1.4	Calibration	6
1.5	Nominal Detector Performance	7
1.6	Electromagnetic Calorimeter Optimisation	7
1.6.1	ECal Transverse Granularity	9
1.6.2	ECal Longitudinal Granularity	12
1.6.3	ECal Active Material	15
1.7	Hadronic Calorimeter Optimisation	16
1.7.1	HCal Absorber Material	17
1.7.2	HCal Transverse Granularity	19
1.7.3	HCal Longitudinal Granularity	21
1.7.4	HCal Sampling Fraction	23
1.7.5	HCal Sampling Frequency	23
1.8	Global Detector Parameters	26
1.8.1	The Magnetic Field Strength	27
1.8.2	Inner ECal Radius	29
1.9	Conclusions	30
2	Energy Estimators	31
2.1	Calibration	31
2.1.1	Calibration in the particle flow paradigm	31
2.1.2	Calibration and detector optimisation	32

2.1.3	Calibration Goals	33
2.1.4	Digitisation	34
2.1.5	MIP Scale Setting	39
2.1.6	Electromagnetic and hadronic scale setting	41
	Bibliography	51
	List of figures	53
	List of tables	57

*“Writing in English is the most ingenious torture
ever devised for sins committed in previous lives.”*

— James Joyce

Chapter 1

Calorimeter Optimisation Studies

“The simple believes everything, but the prudent gives thought to his steps.”

— Proverbs 14:15

1.1 Calorimeter Optimisation Studies

If the future linear collider is to reach its maximum potential in terms of energy resolution then, optimisation of the detector will be essential. The energy resolution in the particle flow paradigm is dependant upon several detector components. The momentum of charged particles arises from the shape of the tracks deposited within the detector while the energy of uncharged particles arise from calorimetric measurements. Application of sophisticated pattern recognition algorithms allows the particle type to be inferred for the charged particles. In turn this allows for the conversion of the track momentum into an energy measure for the charged particles. The particle identification algorithms use the topological information acquired from the calorimetric energy deposited to infer particle type for a subset of charged particles.

The calorimetric energy deposits are therefore used in a twofold manner: (i) as energy measurements for neutral particles and (ii) as input for particle identification algorithms. There is potential for significant gains to be made in physics performance by optimising the calorimeters due to their dominant role in energy measurements. In this chapter the optimisation of the calorimeters is considered. Parameters such

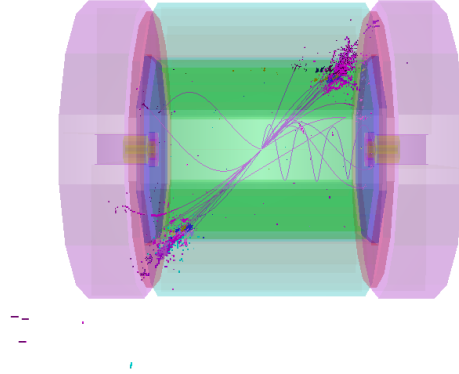


Figure 1.1: 500 GeV di-jet $Z \rightarrow uds$ event display for nominal ILD detector.

as the longitudinal granularity, transverse granularity and material choices for the calorimeters are considered.

This chapter concludes with an optimisation of several global parameters for the detector. These parameters are not calorimeter specific, but the optimisation procedure developed for the calorimeters is appropriate to use. These parameters relate to the global detector size and the magnetic field applied throughout solenoid in the detector.

1.2 Metric

This section describes the various metrics used in these detector optimisation studies.

1.2.1 Jet Energy Resolution

The primary metric used to determine detector performance was the jet energy resolution. This was found through the simulation of off-shell mass Z boson (Z') events decaying to light quarks (u , d , s). In these events the Z' boson is produced at rest, which means the typical decays form two mono-energetic jets that are produced back to back as shown in figure 1.1. Only events where $|\cos(\theta)| < 0.7$, where θ is the polar angle of the quarks from the Z' decay, are used in the metric calculation to ensure little energy is lost down the beam axis. Using these events the jet energy resolution is calculated as follows:

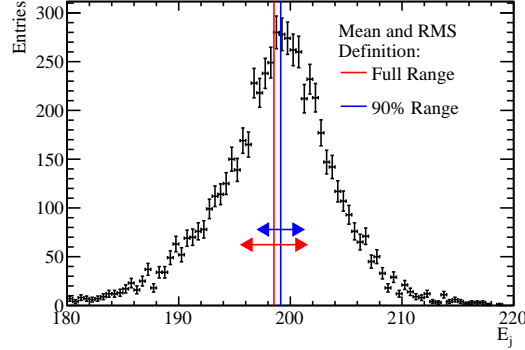


Figure 1.2: Definition of jet energy resolution. Reconstructed jet energy for 200 GeV di-jet $Z \rightarrow uds$ events for nominal ILD detector.

$$\frac{\text{RMS}_{90}(E_i)}{\text{Mean}_{90}(E_i)} = \frac{\text{RMS}_{90}(E_{jj})}{\text{Mean}_{90}(E_{jj})} \times \sqrt{2} \quad (1.1)$$

where $\text{RMS}_{90}(E_{jj})$ and $\text{Mean}_{90}(E_{jj})$ are the root mean squared (RMS) and the mean of the reconstructed energy distribution respectively. A detailed description of this metric and why it is used can be found here [10], however, it is sufficient for this study to note that the reduced range is designed to remove the effect of outliers on the overall detector performance.

An example of the application of this metric can be found in figure 1.2. Using the full range the mean and RMS are 198.5 and 5.8 GeV respectively while using the smallest range containing 90% of the data the mean and RMS are 199.1 and 4.1 GeV respectively. This example indicates that the jet energy resolution is strongly influenced by the outliers in the distribution. Removing these events from the jet energy resolution calculation makes this metric more robust as well as making it more representative of the bulk of the data.

In the subsequent analysis four di-jet/ Z' energies are considered: 91 GeV, approximately the top mass; 200 GeV, is the point at which intrinsic energy resolution and pattern recognition confusion are of comparable size for the nominal ILD detector; 360 GeV, this gives 180 GeV energy jets, which is approximately the top quark mass; and 500 GeV is the nominal running energy for the ILC. Each sample contained 10,000 events generated isotropically so that, given the polar angle cut, approximately 7,000 events contribute to the jet energy resolution metric.

1.2.2 Jet Energy Resolution Decompositions

In several optimisation studies it proved useful to decompose the jet energy resolution into terms describing the intrinsic energy resolution of the detector and the pattern recognition confusion arising from incorrect associations of tracks to calorimetric energy deposits. Pattern recognition confusion manifests itself on energy measurements in two ways:

- If a calorimetric energy deposit from a charged particle is incorrectly associated to its track that energy deposit is double counted.
- If a calorimetric energy deposit from a neutral particle is incorrectly associated to a track the energy deposit is not counted at all.

Both of these lead to inaccurate measurements of the jet energy and thus degrade the resolution.

The decomposition of the jet energy resolution was achieved by cheating various aspects of the reconstruction. The intrinsic energy resolution contribution to the jet energy resolution was determined by fully cheating the pattern recognition as in this case all confusion is negated. The total confusion is defined as the quadrature difference between the jet energy resolution using the standard reconstruction and this fully cheated reconstruction.

Furthermore, it is possible to cheat the pattern recognition associated with individual types of particles. This is particularly useful for studies related to the ECal as, by cheating the photon pattern recognition, it is possible to isolate the confusion associated with photons. The photon confusion is defined as the quadrature difference between the jet energy resolution using the standard reconstruction and the reconstruction where photons pattern recognition is cheated.

The intrinsic energy resolution, total confusion and photon confusion described here are used extensively throughout this chapter.

1.2.3 Single Particle Energy Resolution

As approximately 70% of jet energy arise from charged particle, whose energy measurements are taken from tracks, changes to the intrinsic energy resolution of the

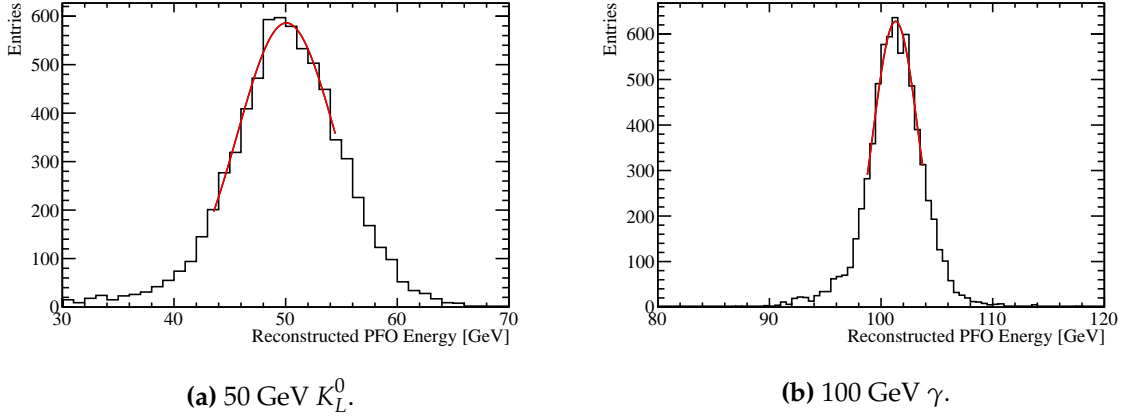


Figure 1.3: Reconstructed energy distribution using nominal ILD detector model.

calorimeters can be washed out when examining the intrinsic energy resolution using jets. Therefore, it occasionally proved useful to consider the single particle energy resolutions as a function of the detector parameter of interest. For ECal related studies γ s were used as the single particle as their energy deposit arise from calorimetric energy deposits that are almost entirely confined to the ECal and similarly K_L^0 s were used for HCal related studies.

For these single particle samples the energy resolution is defined using a Gaussian fit to the reconstructed energy distributions. The fit was applied to the narrowest region of the reconstructed PFO energy distribution that contained at least 75% of the data. This increases the likelihood that the fit converges and ensures a better parameterisation of the bulk of the data set. The resolution is defined as the standard deviation divided by the mean of that reconstructed Gaussian. A total of 10,000 events are used to calculate the energy resolution at each fixed energy point. A cut of $|\cos(\theta)| < 0.7$, where θ is the polar angle of the single particle, is applied to ensure events avoid the Barrel/EndCap overlap region. Examples of the single particle energy distributions for 100 GeV γ s and 50 GeV K_L^0 s alongside the Gaussian fit used to determine their energy resolution are shown in figure 1.3.

1.3 Event Generation, Simulation and Reconstruction

The jet fragmentation and hadronisation for the $Z \rightarrow uds$ events used for determining the metric for detector performance was controlled using PYTHIA [9] that had been

tuned using data from LEP [2]. Single particle spatially isotropic samples of K_L^0 , γ and μ^- were produced for the calibration of each detector model. A simple c++ script was written to generate the relevant HEPevt common blocks for these samples.

Detector model simulation was performed using MOKKA [7], a GEANT4 [1] wrapper providing detailed geometric descriptions of detector concepts for the linear collider. Event reconstruction was performed using MARLIN [5], a c++ framework designed for reconstruction at the linear collider. PandoraPFA [6,10] was used to apply Particle Flow Calorimetry in the reconstruction, the full details of which can be found in chapter PANDORA CHAPTER.

1.4 Calibration

Calibration of the simulated detector models considered in these optimisation studies was critical. Proper calibration allows an unbiased comparison between detector models to be made and the correct conclusions drawn. To that end the calibration procedure described in chapter CALIBRATION CHAPTER ?? was applied to all detector models considered. A brief summary of the purpose of this procedure is given here:

- Digitisation calibration for the ECal and HCal. This ensured an accurate estimation of the energy deposited in the absorber layers in these sampling calorimeters.
- Minimum ionising particle (MIP) scale calibration in the digitiser and PandoraPFA. This ensures that the MIP response was properly set in the digitiser and in PandoraPFA. The digitiser uses this information to place electronic dynamic ranges into the readout technology simulated, while PandoraPFA uses the MIP scale to place cuts to veto noise from the detector.
- Electromagnetic and hadronic scale setting. This ensures that the electromagnetic scale and the hadronic energy scales are properly set within PandoraPFA and hence the output PFOs. The scales differ due to the different shower dynamics governing the growth of electromagnetic and hadronic showers. One key difference is the presence of a missing energy component in hadronic showers.

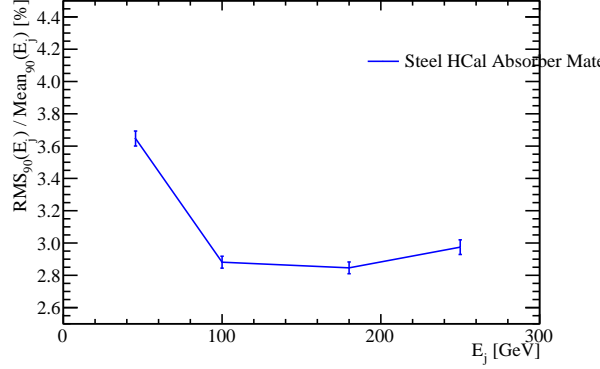


Figure 1.4: Jet energy resolution as a function of jet energy for the nominal ILD detector.

- Retraining photon likelihood data in PandoraPFA. This ensures that the likelihood data used to identify photons in PandoraPFA was retrained for each detector model.

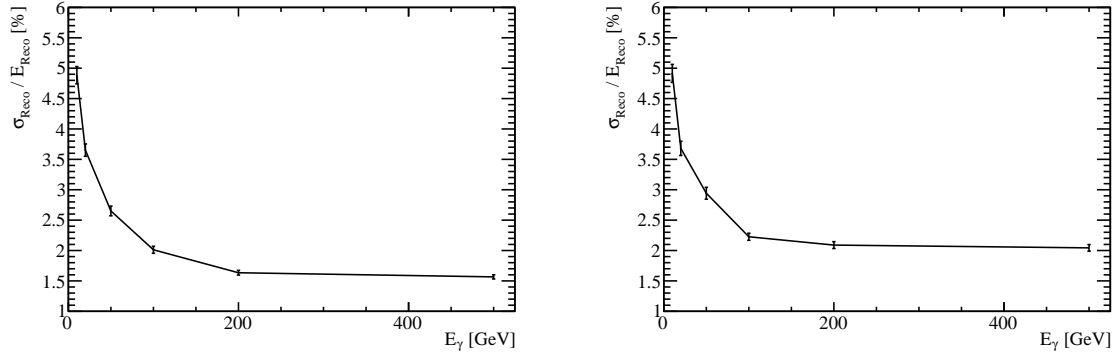
1.5 Nominal Detector Performance

This sections needs more details on nominal ILD configuration.

The energy resolution for single γ and K_L^0 events as a function of the single particle MC energy, for the nominal ILD detector, is shown in figures 1.5 and 1.6 respectively. The jet energy resolution for the nominal ILD detector model can be found in figure 1.4.

1.6 Electromagnetic Calorimeter Optimisation

The ECal primarily measures the energy deposits of electromagnetic showers. The default ILD detector model ECal, summarised in table 1.1, contains 24 radiation lengths (X_0 , which acts to confine all but the highest energy electromagnetic showers within it. The longitudinal structure of this default model is 29 readout layers, consisting of pairs of active and absorber material, and one presampling layer, which exists to encourage shower development. Increasing the thickness of the absorber material part way into the detector reduces the number of readout channels and cost of the overall



(a) Silicon active material, $5 \times 5 \text{ mm}^2$ ECal transverse granularity. (b) Scintillator active material, $5 \times 5 \text{ mm}^2$ ECal transverse granularity.

Figure 1.5: Energy resolution as a function of photon energy for the nominal ILD detector for both the silicon and scintillator options.

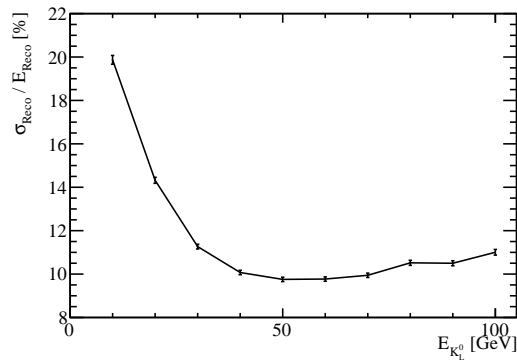


Figure 1.6: Energy resolution as a function of K_L^0 energy for the nominal ILD detector.

calorimeter while retaining a high sampling rate at the start of particle showers, which is crucial for the pattern recognition aspect of particle flow calorimetry.

Parameter	Default Value
Transverse Granularity	$5 \times 5\text{mm}^2$ square cells
Longitudinal Granularity	29 Readout Layers, 1 Presampling Layers
Active Material Choice	Silicon or Scintillator
Active Material Thickness	0.5 mm (Silicon) or 2 mm (Scintillator)
Absorber Material Choice	Tungsten
Absorber Material Thickness	20 Layers of 2.1 mm followed by 9 Layers of 4.2 mm

Table 1.1: Nominal ILD detector model ECal configuration.

The parameters being optimised in this study are:

- Transverse granularity or cell size. This is a vital aspect of the detector in the particle flow paradigm as smaller cell sizes give greater potential for being able to separate energy deposits from charged and neutral particles. This transverse granularity should have little to no effect on the intrinsic energy resolution of the detector.
- Longitudinal granularity or cell depth. This parameter dictates the intrinsic energy resolution of the detector as smaller cell depths mean more sampling is done of the particle shower and so, due to the Poissonian statistics governing the measurement of particle showers, the better the resolution.
- Active material choice. This is a choice between silicon or scintillator. As well as providing different intrinsic energy resolutions the readout mechanics of these two options are significantly different. There is no clear prior knowledge as to which should provide better performance.

1.6.1 ECal Transverse Granularity

For this study a number of different detector models were considered where the transverse granularity in the ECal had been varied about the nominal value of $5 \times 5\text{mm}^2$ square cells. The granularities considered were $3 \times 3\text{mm}^2$, $5 \times 5\text{mm}^2$, $7 \times 7\text{mm}^2$, $10 \times 10\text{mm}^2$, $15 \times 15\text{mm}^2$ and $20 \times 20\text{mm}^2$ square cells for both the silicon and scin-

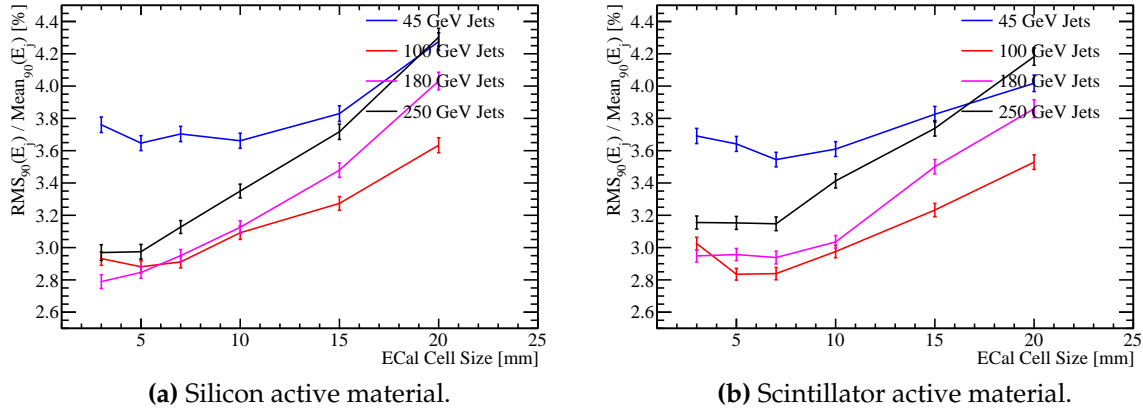


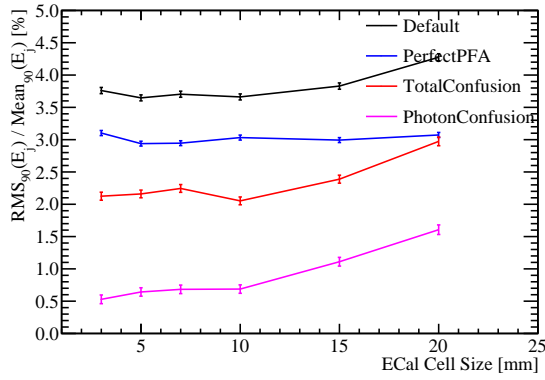
Figure 1.7: Jet energy resolution as a function of ECal cell size for the silicon and scintillator ECal options.

tillator active material options. The jet energy resolution as a function of transverse granularity in the ECal is shown in figure 1.7.

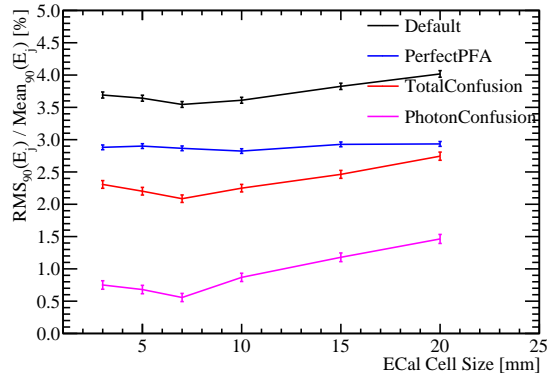
The jet energy resolution was found to improve with decreasing cell size. This is expected as smaller cell size lead to better separation of energy deposits from neutral and charged particle showers.

By examining the breakdown of the jet energy resolution into intrinsic resolution and confusion terms, as explained in chapter BLAH, it is possible to conclude that the dominant factor affecting the jet energy resolution when the transverse granularity of the ECal is varied is the confusion arising from photon energy deposits. Examples of jet energy resolution breakdowns are shown for 45 and 250 GeV jets for both the silicon and scintillator ECal options in figure 1.8. As expected in the intrinsic energy resolution does not change significantly with the transverse granularity.

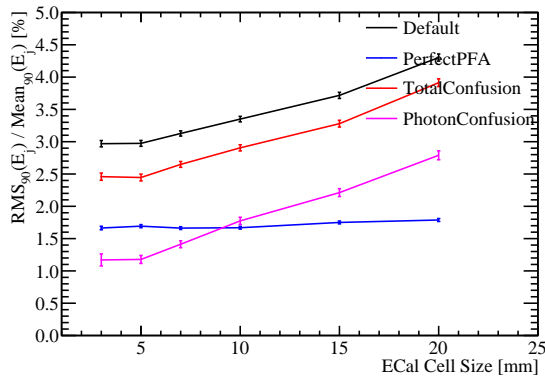
A more targeted test of the intrinsic energy resolution of the ECal is presented in figure 1.9, which examines the energy resolution of single photon samples at 100 GeV. For the silicon option the intrinsic energy resolution was found to not vary significantly across the transverse granularities under consideration, however, there is a degradation in energy resolution with increasing cell size for the scintillator option. This originates from an inactive region of material in the simulation that represents the multi pixel photon counter (MPPC). The MPPC occupies a fixed area of the cell irrespective of cell size and so fractionally the "dead" region of the cell increases as cell size is reduced (cite this somehow). These trends will be present in the jet energy



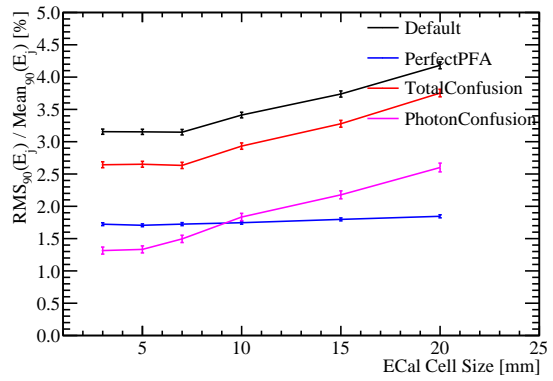
(a) Silicon active material, 45 GeV Jets.



(b) Scintillator active material, 45 GeV Jets.



(c) Silicon active material, 250 GeV Jets.



(d) Scintillator active material, 250 GeV Jets.

Figure 1.8: Jet energy resolution breakdown as a function of ECal transverse granularity for 45 and 250 GeV jets. Results are given for both the silicon and scintillator ECal options.

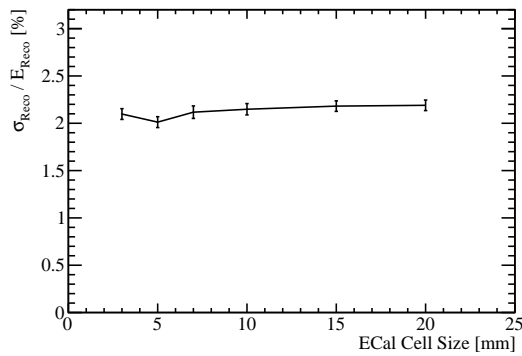
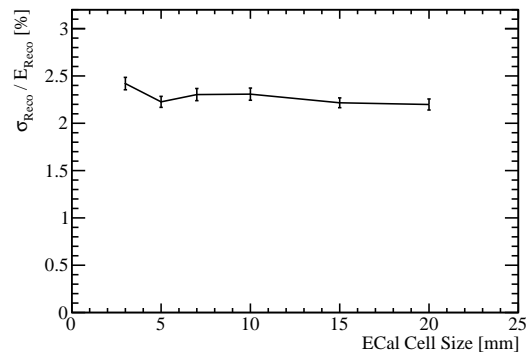
(a) Silicon active material, 100 GeV γ .(b) Scintillator active material, 100 GeV γ .

Figure 1.9: Energy resolution as a function of ECal transverse granularity for 100 GeV photons. Results are given for both the silicon and scintillator ECal options.

resolution studies, however, as only a small fraction, $\approx 10\%$, of the jet energy arises from the ECal these trends will be washed out when looking purely at jets.

In conclusion smaller transverse granularities in the ECal significantly improve the jet energy resolution for both the silicon and scintillator options. The intrinsic energy resolution of the ECal is largely invariant to changes in the transverse granularity for the silicon option, while larger transverse granularities are beneficial to the scintillator option as they reduce the impact of "dead" regions of the detector.

1.6.2 ECal Longitudinal Granularity

The performance of a number of detector configurations was examined where the longitudinal granularity of the ECal absorber material had been varied about the nominal value. This study was performed for both the silicon and scintillator active material options. In all cases considered tungsten was used as the absorber material in the ECal and the active layer thicknesses were not changed, that is 0.5 mm for the silicon option and 2 mm for the scintillator option. The layout of the ECal for detector models considered are summarised in table 1.2. For each detector model considered in this study the total number of radiation lengths in the ECal is kept approximately constant. This is done by varying the thickness of the absorber material when modifying the number of layers in the ECal.

Total Number of Layers $N_{\text{Layers ECal}}$	N_{Layers} Region 1	Absorber Thickness Region 1 [mm]	N_{Layers} Region 2	Absorber Thickness Region 2 [mm]	Total Thickness [X_0]
30	20	2.10	9	4.20	22.77
26	17	2.40	8	4.80	22.60
20	13	3.15	6	6.30	22.47
16	10	4.00	5	8.00	22.31

Table 1.2: Transverse granularity layout of the ECal models considered. Radiation length of tungsten absorber is 3.504mm [8]. Note that the presampler layer contributes one layer to the cumulative number of layers value for all detector models considered.

The jet energy resolution was found to improve with increasing longitudinal granularity. This is expected as a more layers in the calorimeter, for the same total thickness,

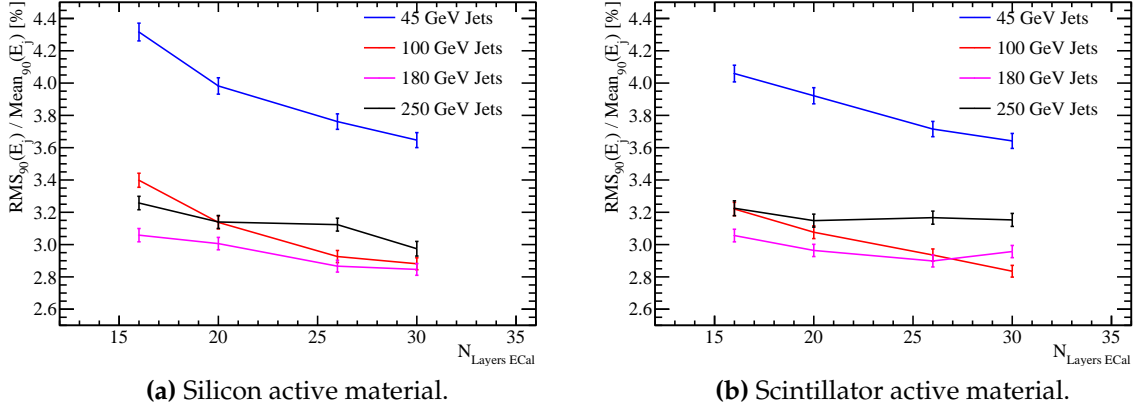


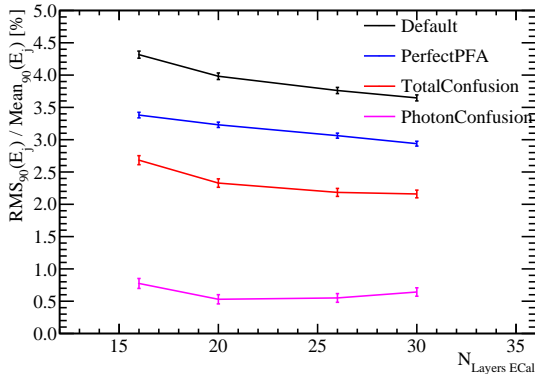
Figure 1.10: Jet energy resolution as a function of longitudinal granularity in the ECal for the silicon and scintillator ECal options.

implies greater sampling of the particle shower and so, as the energy resolution obeys Poissonian statistics, an improvement in the intrinsic energy resolution is observed. A particularly strong dependancy on ECal longitudinal granularity is noted at low energies, but this reduces significantly as energies rise.

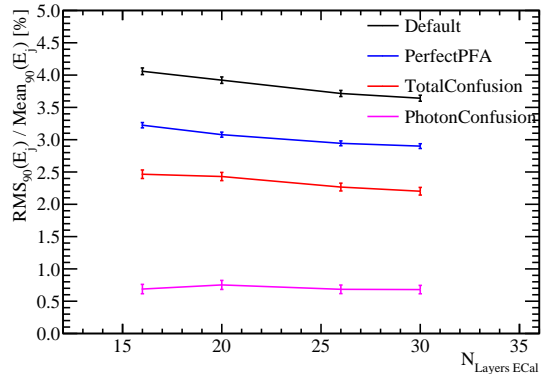
The strong dependancy of the jet energy resolution on the ECal longitudinal granularity can be expanded upon by looking at the decomposition of the jet energy resolution, which is shown in figure 1.11 for the 45 and 250 GeV energy jets. At low energies the trend is twofold: an improvement to the intrinsic energy resolution with more sampling of particle showers and a reduction in the impact of confusion. For high energy jets, where confusion dominates, there is little to no change in the intrinsic energy resolution and confusion as a function of ECal transverse granularity.

Further understanding is gained by considering the energy resolution of single photon samples at 100 GeV as a function of the longitudinal granularity in the ECal, which is shown in figure 1.12. At these large photon energies it is clear that the intrinsic energy resolution of the ECal is improved by having finer longitudinal segmentation in the ECal. This trend will be present in the jet energy resolution study, but as only $\approx 10\%$ of the jet energy is measured in the ECal in comparison to $\approx 100\%$ of the photons energy, it will be obscured by the energy resolution of the rest of the detector, which is invariant to the ECal longitudinal segmentation.

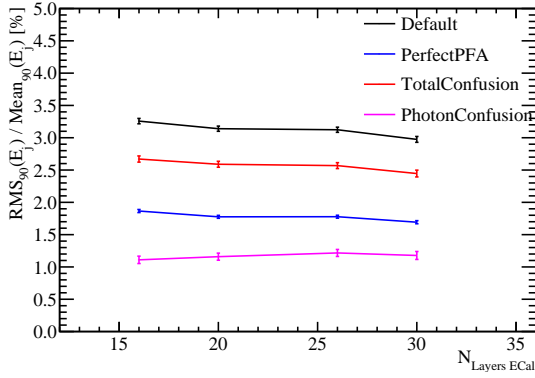
The intrinsic energy resolution of the ECal is improved by having a finer transverse granularity. This is evident when looking at the energy resolution of photons



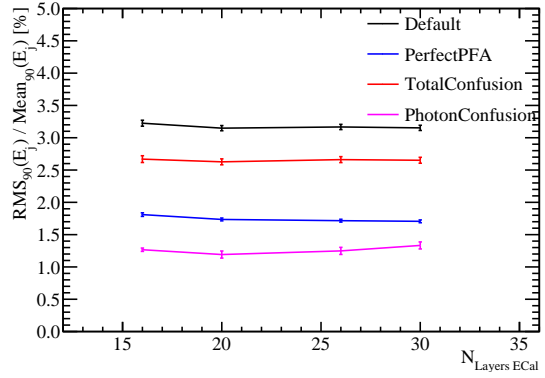
(a) Silicon active material, 45 GeV Jets.



(b) Scintillator active material, 45 GeV Jets.



(c) Silicon active material, 250 GeV Jets.



(d) Scintillator active material, 250 GeV Jets.

Figure 1.11: Jet energy resolution breakdown as a function of ECal longitudinal granularity for 45 and 250 GeV jets. Results are given for both the silicon and scintillator ECal options.

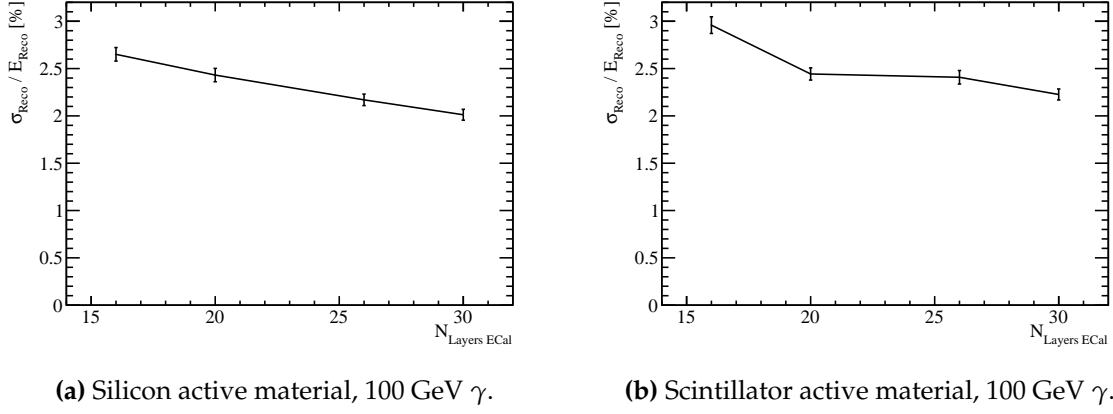


Figure 1.12: Energy resolution as a function of function of ECal longitudinal granularity for 100 GeV photons. Results are given for both the silicon and scintillator ECal options.

whose energy deposits are localised within the ECal. This trend is again clear when considering the energy resolution of low energy jets, however, at higher energies the longitudinal granularity in the ECal is not a significant factor in determining detector performance.

1.6.3 ECal Active Material

In sections 1.6.1 and 1.6.2 the performance of the ECal was reported for both the silicon and scintillator options and to a large extent the performance of the two options was the same. There were a few differences, which attention should be brought to:

- The intrinsic energy resolution of a silicon ECal is worse than that of a scintillator ECal for low energies, while the trend is reversed at high energies. The cross over point in performance occurs between 20 and 50 GeV. This trend is shown in figure 1.5.
- The "dead" region due to the presence of the MPPC in the scintillator option degrades performance of the detector for small transverse granularities. No such effect is seen for the silicon option. This effect is shown in figure 1.9.

The lack of this "dead" region of the detector and the beneficial intrinsic energy resolution at large energies indicates a preference for a silicon detector, however, there is no clear preference based on these studies.

1.7 Hadronic Calorimeter Optimisation

The HCal is designed to measure the energy deposits from hadrons. The default ILD detector model HCal, summarised in table 1.3, contains ≈ 6 nuclear interaction lengths (λ_I). The ECal contributes approximately one λ_I giving a total of $\approx 7\lambda_I$, which is sufficient to confine the bulk of jets up to 1 TeV events, which is the maximum running energy for the ILC. The longitudinal structure of this model consists of 48 readout layers each containing a 3 mm active layer of scintillator and a 20 mm absorber layer of iron. There are several readout technology options under consideration for the HCal, which are analogue, digital and semi-digital, however, for this study only the analogue HCal is considered.

Parameter	Default Value
Transverse Granularity	$30 \times 30\text{mm}^2$ square cells
Longitudinal Granularity	48 Readout Layers
Active Material Choice	Scintillator Tiles
Active Material Thickness	3 mm
Absorber Material Choice	Steel
Absorber Material Thickness	20 mm

Table 1.3: Nominal ILD detector model HCal configuration.

The parameters being optimised in this study are:

- Transverse granularity or cell size. This is key to successful application of pattern recognition in the particle flow paradigm, but should not change intrinsic energy resolution.
- Longitudinal granularity or cell depth. This governs the intrinsic energy resolution of a calorimeter.
- Depth of calorimeter. This is important in determining the impact of leakage of energy out of the detector.
- Sampling fraction. This is the ratio of the active medium thickness to the absorber medium thickness. As sampling calorimetry is based on sampling of particle showers it is expected that this is an important parameter. However, above a given sampling fraction there should be little difference between performance if

showers are sampled at a high enough rate to get a good estimate of the incoming particles energy.

- Absorber material choice. This is a choice between steel or tungsten. While this does not change the active medium choice it does dictate the growth and propagation of showers and so plays a crucial role in calorimetry. While tungsten is more expensive than steel for the raw material the larger number of interaction lengths per length scale for tungsten mean that it is possible to create a smaller detector with the same number of interaction lengths within it. This reduces the size of the solenoid needed to generate the magnetic field and so lowers the price of the detector. As both of these materials are viable as absorber medium choices it is crucial to determine if either is more advantageous from a physics perspective.

1.7.1 HCal Absorber Material

The nominal choice of absorber material is steel, tungsten provides a feasible alternative material. While more expensive than steel, tungsten contains more radiation lengths per unit length than steel and so the overall size of the detector would reduce meaning the solenoid could be smaller, which would to first order offset the additional cost of the tungsten. This section aims to determine whether either of these options is beneficial when considering the jet energy resolution of the detector.

In this study the total depth of absorber material, in nuclear interaction lengths, was held constant for both models. This was to ensure any performance changes were not due to additional material as opposed to the intrinsic energy resolutions of the absorber materials. The interaction of hadrons with the absorber material within the detector is simulated by GEANT4. The model for these interactions is dependent upon the choice of physics list, which by default is the QGSP_BERT physics list. This list is recommended by the GEANT4 authors to use for high energy physics calorimetry as it gives good agreement between experiment. For this study both the QGSP_BERT and the QGSP_BERT_HP physics lists are tested. The QGSP_BERT_HP list uses the high precision neutron package (NeutronHP) to deal with the transportation of neutrons from below 20 MeV to thermal energies. This added detail was thought to be necessary for a study involving tungsten due to the increased time of shower development.

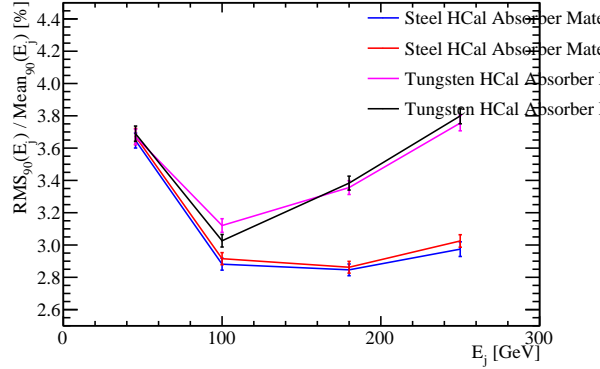


Figure 1.13: Jet energy resolution as a function of jet energy for various absorber materials in the HCal and physics lists.

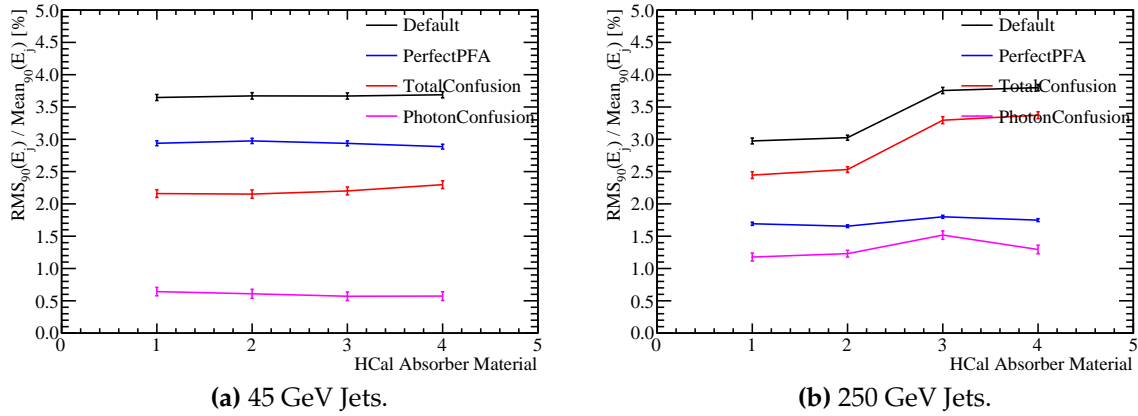


Figure 1.14: Jet energy resolution breakdown as a function of HCal absorber material and physics list for 45 and 250 GeV jets.

The jet energy resolution for the steel and the tungsten HCal options, for using both the QGSP_BERT and the QGSP_BERT_HP physics lists, are shown in figure 1.13 as a function of jet energy. These results indicate that steel outperforms tungsten as an absorber material, particularly for high energy jets. At low energies the performance is similar, indicating that the intrinsic energy resolution of the two options is comparable. The use of the QGSP_BERT_HP physics list, as opposed to QGSP_BERT, has a minimal impact on these results.

Expanding upon this further by examining the jet energy resolution breakdowns as shown in figure 1.14, it can be seen that the change in performance when changing the HCal absorber material from steel to tungsten is due to changes in the confusion. The change in confusion is most likely due to the fact that the PandoraPFA algorithms

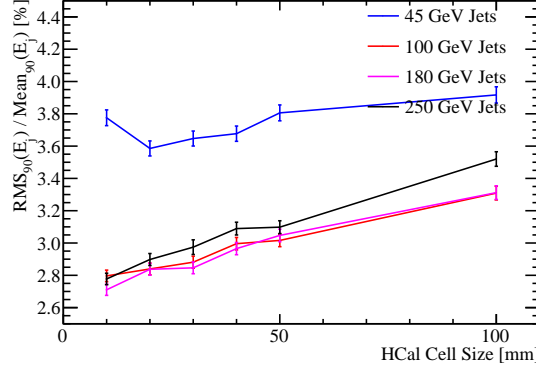


Figure 1.15: Jet energy resolution as a function of HCal cell size.

are tuned for HCal cell dimensions based on the steel HCal option, while the HCal cells for the tungsten option HCal will be smaller by a factor of approximately 1.7 ($\approx 16.77/9.946$). The jet energy resolution breakdowns also indicate that the intrinsic energy resolution of the tungsten HCal is marginally worse, particularly for high energy jets, than that of a steel HCal.

In conclusion, the steel option HCal outperforms the tungsten option in terms of intrinsic energy resolution and pattern recognition confusion making it the more preferred option of the two.

1.7.2 HCal Transverse Granularity

For this study a number of different detector models were considered where the transverse granularity in the HCal had been varied about the nominal value of $30 \times 30 \text{ mm}^2$ square cells. The granularities considered were $10 \times 10 \text{ mm}^2$, $20 \times 20 \text{ mm}^2$, $30 \times 30 \text{ mm}^2$, $40 \times 40 \text{ mm}^2$, $50 \times 50 \text{ mm}^2$ and $100 \times 100 \text{ mm}^2$ square cells. The jet energy resolution as a function of transverse granularity in the HCal is shown in figure 1.15.

As with the case for the ECal, the jet energy resolution was found to improve with decreasing cell size as smaller cell size lead to better separation of energy deposits from neutral and charged particle showers.

The jet energy resolution breakdowns, shown in figure, 1.16, show that the confusion term varies when changing the HCal transverse granularity, but the intrinsic energy resolution does not. Furthermore, the photon confusion is invariant to changes in HCal transverse granularity, indicating that the observed overall performance

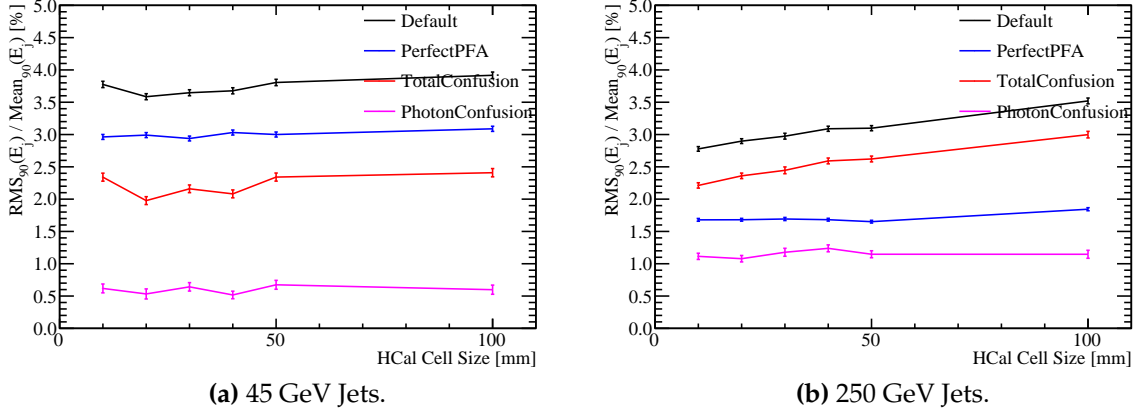


Figure 1.16: Jet energy resolution breakdown as a function of HCal transverse granularity for 45 and 250 GeV jets.

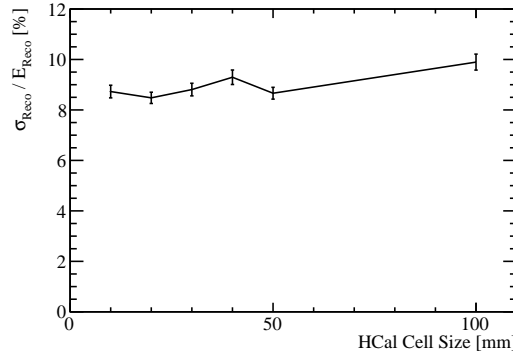


Figure 1.17: Energy resolution as a function of HCal transverse granularity for 50 GeV K_L^0 .

changes are due to the effects of confusion arising from energy deposits from charged and neutral hadrons. Once again for 45 GeV jets the detector performance is dominated by intrinsic energy resolution and so HCal transverse granularity has little effect, while for 250 GeV jets the performance is dominated by confusion and HCal transverse granularity becomes more significant.

The energy resolution of single long lived neutral kaons, K_L^0 , at 50 GeV is considered as a function of transverse granularity in the HCal. This is shown in figure 1.17 and, as expected, the energy resolution of the detector is largely invariant to changes in the transverse granularity in the HCal. As these K_L^0 samples may deposit energy in the ECal, this figure represents the intrinsic energy resolution of the ILD detector as a whole and not purely that of the HCal. However, it is expected that the bulk of the

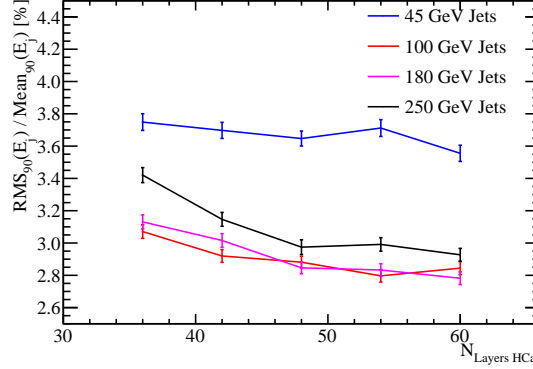


Figure 1.18: Jet energy resolution as a function of number of layers in the HCal.

energy deposited by these samples occurs within the HCal and so such plots are a useful representation of the HCal performance.

The transverse granularity of the HCal acts to determine the impact of confusion from charged and neutral hadron energy deposits. It does not vary the intrinsic energy resolution of the detector, nor does it impact the reconstruction of photons. As confusion is dominant at high jet energies the HCal transverse granularity gains an increasing role in determining detector performance as the energy in an event increases.

1.7.3 HCal Longitudinal Granularity

This section focuses upon change in detector performance when varying the number of layers in the HCal. For this study, the absorber and active layer thicknesses are not varied when adding or subtracting layers from the HCal, so both the total depth of the HCal as well as the number of sampling points of the hadronic showers varies simultaneously, this is in comparison to the study described in section 1.7.5 where the total depth of the HCal is fixed. The detector models considered had 36, 42, 48, 54 and 60 layered HCals.

The jet energy resolution for the various detector models considered is shown in figure 1.24. It was found that increasing the number of layers in the HCal improved the jet energy resolution for high energy jets, while for low energy jets no the performance change was observed. The breakdown of the jet energy resolution for the high energy

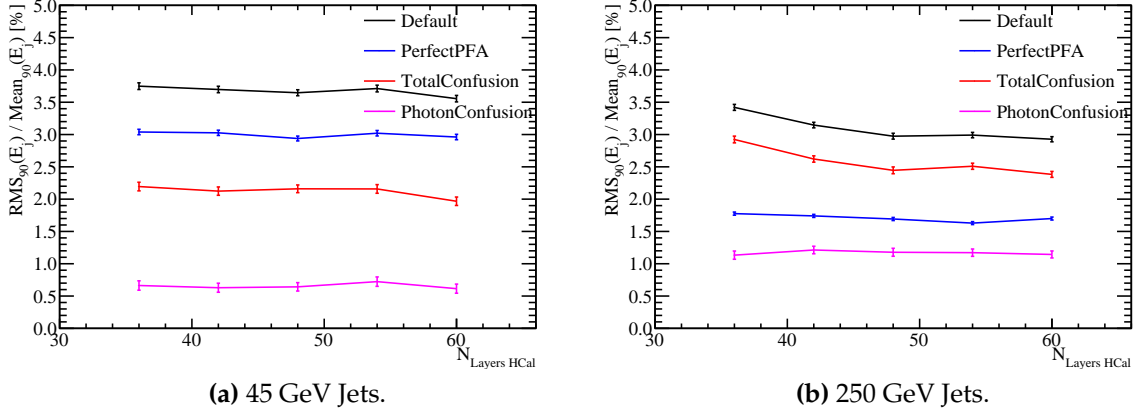


Figure 1.19: Jet energy resolution breakdown as a function of number of layers in the HCal for 45 and 250 GeV jets.

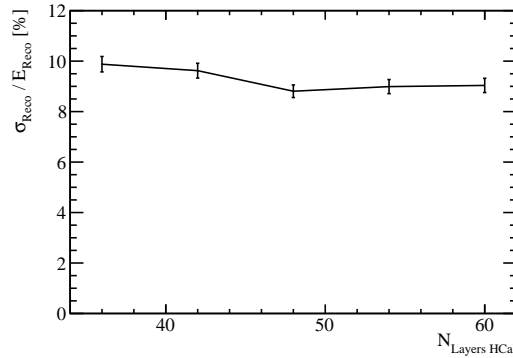


Figure 1.20: Energy resolution as a function of number of layers in the HCal for 50 GeV K_L^0 .

jets, shown in figure ??, indicates a reduction in the confusion term is driving the change in performance when increasing the number of layers in the HCal.

While the intrinsic energy resolution for jets appeared largely invariant to changes in the number of layers in the HCal, it can be seen that there is an associated improvement in the energy resolution for neutral hadrons, which can be seen in figure 1.20. This change in neutral hadron energy resolution will be masked in the jet energy resolution study as only $\approx 10\%$ of the energy of a jet arises from neutral hadrons and the energy resolution change is minimal.

In conclusion, a larger number of layers in the HCal is beneficial to detector performance both in terms of a reduction in pattern recognition confusion as well as an improvement in the energy resolution of neutral hadrons. These performance changes

at the energies considered are relatively small and so it would be feasible to consider changes to the nominal number of HCal layers. However, at higher energies these conclusions could be significantly modified as leakage dominates.

1.7.4 HCal Sampling Fraction

In this section the sampling fraction, the ratio of the active to absorber layer thicknesses were considered. For all detector models considered in this section the total number of nuclear interaction lengths in the HCal was held constant, as was the number of layers in the HCal and the transverse granularity. The detector models considered are summarised in table 1.4.

Sampling Fraction	Absorber Thickness [mm]	Active Thickness [mm]
0.05	20.430	1.022
0.10	20.213	2.021
0.15	20.000	3.000
0.20	19.792	3.958
0.25	19.587	4.897

Table 1.4: Sampling fraction of HCal models considered.

The jet energy resolution for these detector models is shown in figure 1.24. It was found that there is no significant change in performance when varying the sampling fraction.

1.7.5 HCal Sampling Frequency

This section aims to determine the change in performance when the sampling frequency, the number of times a particle shower is sampled per unit length, in the HCal is varied. This was done by varying the number of readout layers, while maintaining the total number of nuclear interaction lengths contained within the HCal. In all cases the absorber material was steel while the active material was scintillator. Each HCal configuration had the same total number of nuclear interaction lengths, $5.72 \lambda_I$ in the absorber material and $0.19 \lambda_I$ in the active material, however, the thickness of the

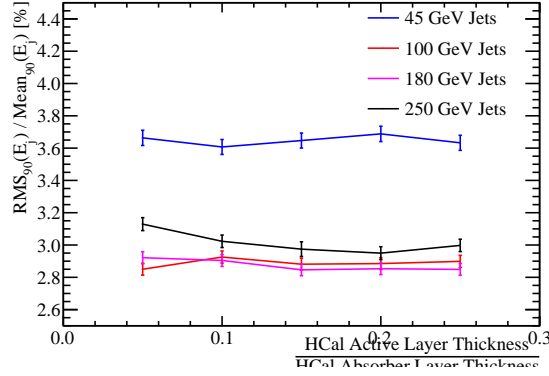


Figure 1.21: Jet energy resolution as a function of sampling frequency in the HCal. Label needs fixing.

layers was varied depending on the total number of layers being considered. The ratio of the active material layers to the absorber material layers, the sampling fraction, was also kept constant in this study. A summary of the detector models considered in this study can be found in table 1.5.

Number $N_{\text{Layers HCal}}$	Absorber Thickness [mm]	Active Thickness [mm]
60	16.00	2.40
54	17.78	2.67
48	20.00	3.00
42	22.86	3.43
36	26.67	4.00
30	32.00	4.80
24	40.00	6.00
18	53.33	8.00

Table 1.5: Transverse granularity layout of various HCal models considered.

The jet energy resolution for the various detector models considered is shown in figure 1.24. It was found that increasing the number of layers in the HCal, for the same total thickness, improved the jet energy resolution for all jet energies considered. Based on the increase in the frequency of sampling of particle showers in the HCal, it is expected that the intrinsic energy resolution of the detector should improve. However,

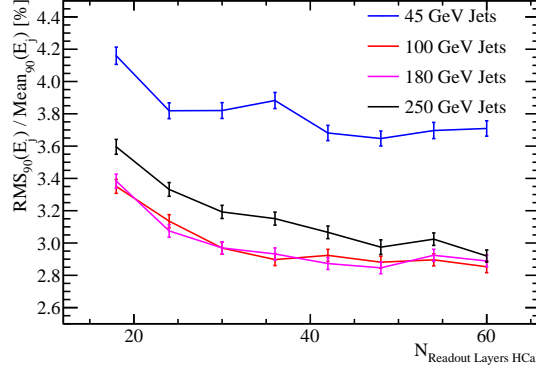


Figure 1.22: Jet energy resolution as a function of sampling frequency in the HCal.

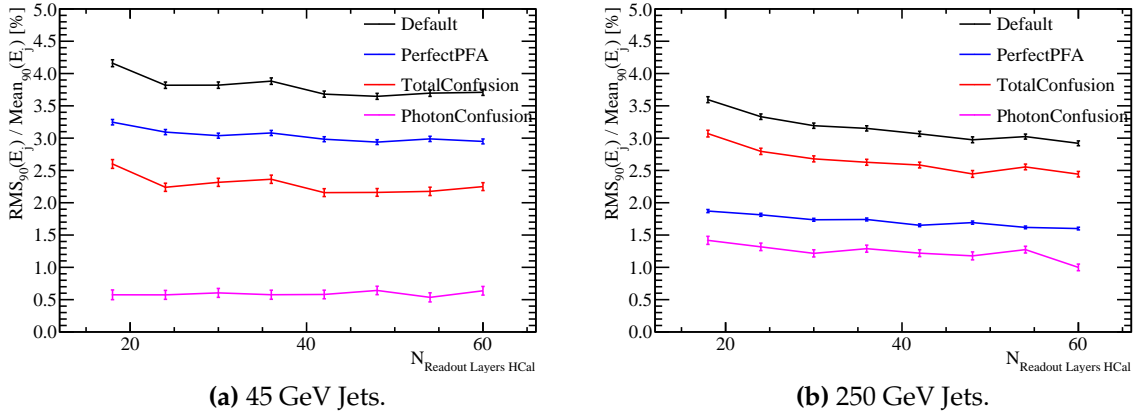


Figure 1.23: Jet energy resolution breakdown as a function of HCal sampling frequency for 45 and 250 GeV jets.

the improvement observed in jet energy resolution for high energy jets indicates that sampling frequency is also affecting the confusion terms.

These trends are further explored by considering the breakdown of jet energy resolution, which are shown in figure 1.23. As expected from the standard performance reconstruction trends as a function of jet energy, there is an improvement in both the intrinsic energy resolution and a reduction in the impact of confusion when the number of layers in the HCal is increased. The dominant trend driving the overall detector performance is that associated with the confusion of separating energy deposits from charged and neutral particles. This emphasises the importance of pattern recognition to detector performance in the particle flow paradigm.

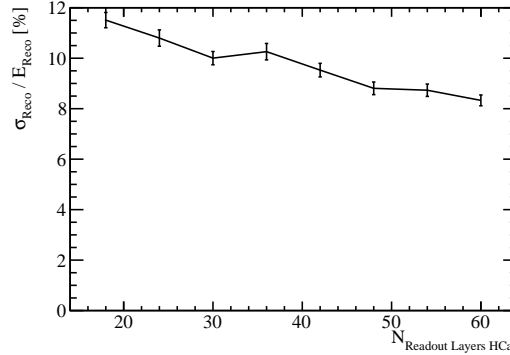


Figure 1.24: Energy resolution as a function of HCal sampling frequency for 50 GeV K_L^0 .

The change in the intrinsic energy resolution of the HCal when varying the sampling frequency is best summarised by looking at the energy resolution of neutral hadrons. A plot of energy resolution against the number of readout layers in the HCal for 50 GeV K_L^0 can be found in figure 1.24. This data shows that a reduction in sampling frequency of a particle shower that accompanies a reduction in the number of readout layers results in a broadening of energy distributions and a degradation in the resolution. It should again be emphasised that these results are for the full ILD detector model and so include the effect of the $\approx 1\lambda_I$ in the ECal.

The increasing the HCal sampling frequency has a twofold effect on the detector performance: an increase in sampling rate of particle showers and an improvement to the intrinsic energy resolution and a reduction in the confusion arising from associating energy deposits from hadrons.

1.8 Global Detector Parameters

This section focuses upon optimisation of two global detector parameters; the magnetic field strength and the ECal inner radius. While these are not directly related to the calorimeter they will both effect detector performance and so were deemed worthy of study alongside the calorimeter parameters.

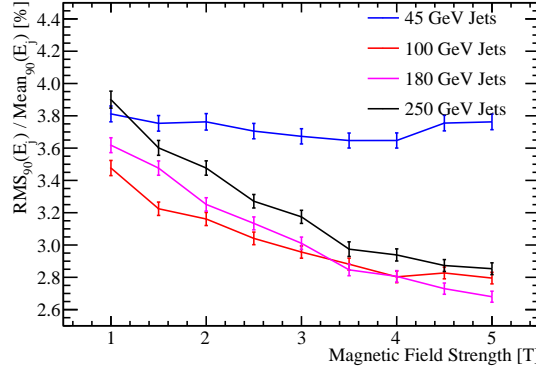


Figure 1.25: Jet energy resolution is shown for several fixed energy jets as a function of magnetic field strength.

1.8.1 The Magnetic Field Strength

The magnetic field is vital to the successful application of particle flow calorimetry. Any charged particles passing through the detector transverse helices that, once reconstructed, can be fitted to give the momentum and so energy of said particle in the particle flow paradigm. The magnetic field also created a separation between charged and neutral hadrons energy deposits in the calorimeters. The larger the magnetic field, the greater this separation and the easier to avoid confusion associate tracks to the correct energy deposits in the calorimeters, which is crucial for particle flow.

The magnetic field strengths considered in this study ranged from 1 to 5 T in steps of 0.5 T. The jet energy resolutions as a function of magnetic field strength, shown in figure 1.25, shows that the jet energy resolution decreases with increasing magnetic field strength for high energy jets. At low energies the performance is largely invariant to magnetic field strength.

Examination of the decompositions of the jet energy resolution, found in figure 1.26, highlights a number of effects.

The first is a clear reduction in confusion with increasing magnetic field strength. This is due to a larger separation between charged and neutral hadron energy deposits in the calorimeter as was expected.

Secondly there is a reduction in intrinsic energy resolution with increasing magnetic field strength for low energy jets, while for high energy jets this trend is reversed. At low energies the momenta of the charged particles will be low and so the radii

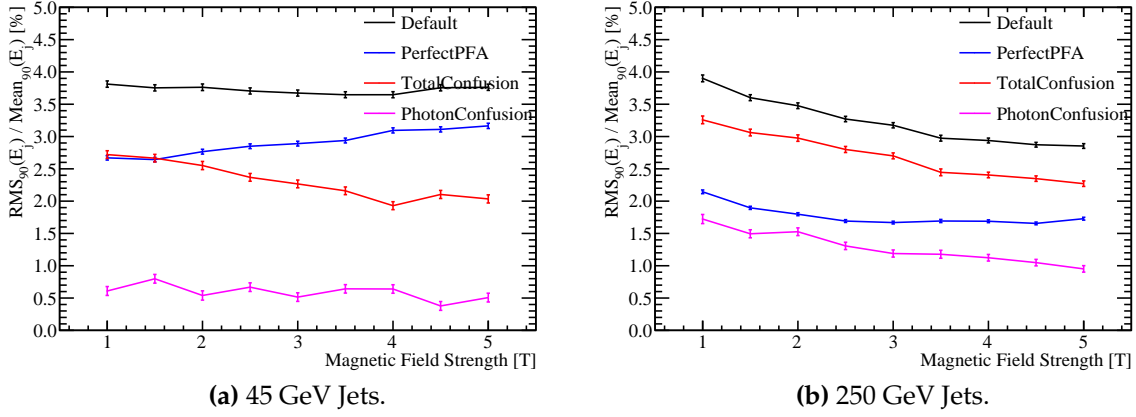


Figure 1.26: Jet energy resolution breakdown as a function of magnetic field strength for 45 and 250 GeV jets.

of curvature of the helix these particles transverse will be small. If the radius for a given particle is small enough it will not make it into the calorimeters. In this case only if the track produced from this particle passes tight selection cuts designed to ensure the track originates from the impact point will the track be used to create a PFO. Therefore, energy can and will be lost in from events where PFOs are stuck within the tracker. Given the radii of curvature is inversely proportional to the magnetic field strength, the larger the magnetic field strength the more tracks will be confined to the tracker. The more tracks that are confined to the tracker, the worse the intrinsic energy resolution becomes as inevitably some tracks fail the quality cuts to form PFOs. At high jet energies the transverse momentum of the particles will be sufficiently large that the radii of curvatures of the helices formed by charged particles will be enough so that they reach the calorimeters on average. However, for low magnetic field strengths more particles deposit energy within the same calorimeter cells. The intrinsic energy resolution plot is determined by associating a single MC particle to each calorimeter cell. At high jet energies and low magnetic field strengths many of the cells will have energy deposits split between multiple cells and so associating a single MC particle per cell is inaccurate. This explains why the intrinsic energy resolution degrades slightly in this scenario. These results are still of interest, however, because the driving term in the jet energy resolution as a function of magnetic field strength is the confusion.

In summary, increasing the magnetic field strength is beneficial to detector performance as it reduces confusion from associating tracks to calorimetric energy deposits from charged particles. While there is a reduction in the intrinsic energy resolution

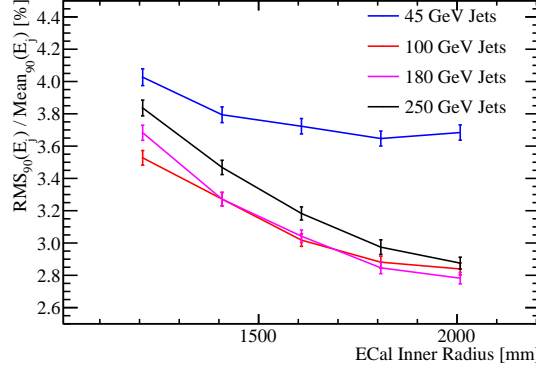


Figure 1.27: Jet energy resolution is shown for several fixed energy jets as a function of ECal inner radius.

for low transverse momentum jets with increasing magnetic field strength, this effect is largely offset by the change in confusion. While the nominal field of 3.5 T gives good performance increasing the field strength is a clear way of making large gains in detector performance.

1.8.2 Inner ECal Radius

This section focuses on optimising the inner ECal radius, or the outer tracker radius. The nominal detector model has an ECal inner radius of 1808 mm and for this optimisation detector models were considered where the ECal inner radii was set to 1208, 1408, 1608 and 2008 mm. All other detector parameters identical to those of the nominal ILD detector model.

The jet energy resolution as a function of ECal inner radius is shown in figure 1.27 and these results show that a large ECal inner radius was highly beneficial to detector performance. This is due to the fact that a large tracker gives more time for charged particles to bend due to the magnetic field, which creates a larger separation between calorimetric energy deposits from charged and neutral particles. This larger separation reduces the confusion when associating calorimetric energy deposits to tracks and so improves the detector performance. This conclusion is backed up by the decomposition of the jet energy resolution for the low and high energy jets, shown in figure ??, which explicitly show a reduction in confusion with increasing ECal inner radius.

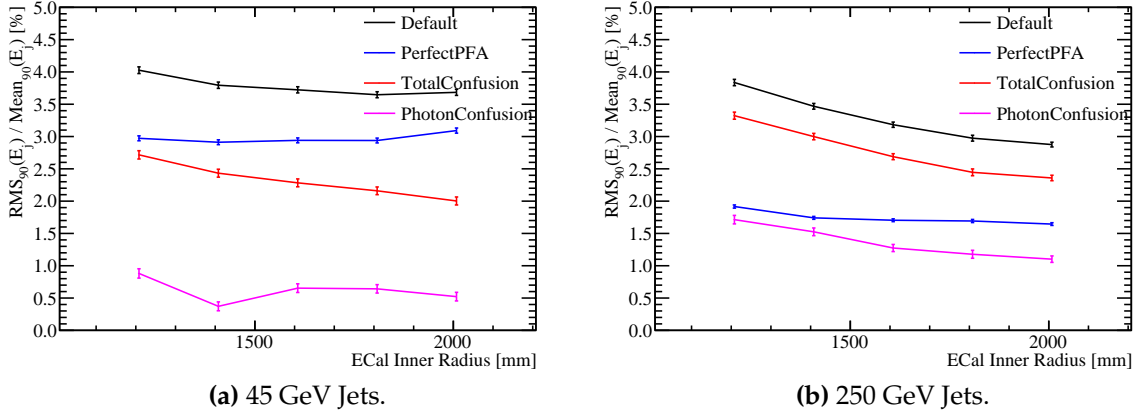


Figure 1.28: Jet energy resolution breakdown as a function of ECal inner radius for 45 and 250 GeV jets.

The intrinsic energy resolution of the detectors follows the same pattern as was observed in the magnetic field study. For low energy jets the larger ECal radius means fewer particles make it to the calorimeters and so some PFOs are not reconstructed giving a worse energy resolution. While at larger jet energies the radii of curvature of the charged particles is sufficiently large as the particles have higher momenta, meaning very few are confined to the tracker and so the intrinsic energy resolution is largely invariant. There is a small degradation in intrinsic energy resolution at low ECal inner radii due to the association of a single MC particle per calorimeter cell when running the cheated pattern recognition as explained in section 1.8.1. Again, this effect has little bearing on the final conclusions as the change in intrinsic energy resolution across the detector models is a second order effect.

In conclusion, increasing the ECal inner radius benefits the jet energy resolution significantly. This trend is driven by changes to the confusion in associating tracks to calorimetric energy deposits, with a larger ECal inner radius producing a reduction in the confusion as separation of charged and neutral particle energy deposits increases.

1.9 Conclusions

Chapter 2

Energy Estimators

“There, sir! that is the perfection of vessels!”

— Jules Verne, 1828–1905

2.1 Calibration

2.1.1 Calibration in the particle flow paradigm

TODO: Trim down.

In any experiment, calibration is essential for ensuring reliability in measured quantities and the linear collider will be no exception to this. At the linear collider there will be several measured quantities each of which will be converted into a measure of the energy deposited in a given region of the detector. These fall into two distinct classes (i) calorimeter energy deposits and (ii) track deposits. The focus of this section will be on the energy deposits in the calorimeter and the procedure developed to ensure that they are reliable.

Calorimeter energy deposits are an essential building blocks for the application of the particle flow paradigm. The separation of energy deposits from charged and neutral particles in the calorimeters is crucial to achieve the full potential of particle flow and this is only possible with accurate energy estimators for those energy deposits. A robust calibration scheme has been developed and will be discussed in the following chapter.

The other crucial energy deposit used in particle flow calorimetry are track energy deposits. These are also crucial to physics performance, however, in the particle flow paradigm these energy deposits are topologically related to the energy of the reconstructed particle. A spatial helix fit is applied to the track energy deposits which when combined with knowledge of the magnetic field yields the momentum of the particle producing the track. Therefore, there is no direct relationship between the energy deposited by the monte-carlo particle in the active medium and the energy of the reconstructed energy. Therefore, precise calibration of the energy deposited by a charged particle track is less crucial than for calorimeter energy deposits. For this reason the focus of this chapter is on the calibration of calorimeter energy deposits.

Calibration of the linear collider simulation extends beyond the raw calorimeter hits and into the particle flow algorithm itself. The fine calorimeter granularity required for particle flow calorimetry yields excellent physical separation of hadronic and electromagnetic showers. Thanks to sophisticated particle identification occurring within PandoraPFA it is possible to distinguish hadronic and electromagnetic showers, which allows for distinct treatments of the hadronic and electromagnetic energy estimators. This distinction can be used to produce a response from the calorimeter that is compensating despite the intrinsic response being non-compensating. A compensating calorimeter would give significant improvements to the energy resolution for the detector.

Two treatments designed to achieve a compensating response from the calorimeters are discussed. The both involve rescaling the energies, the first rescaling is applied using a series of fixed energy independent constants, while the second uses the energy density of the calorimeter hits in the shower to determine the energy rescaling factor.

2.1.2 Calibration and detector optimisation

Optimising the detector at a future linear collider will be crucial to exploit the full physics potential available to it. An extensive optimisation of the calorimeters was performed and the results can be found in chapter 1.1. For each detector model considered in this study the calibration procedure outlined in this section was applied to ensure optimal performance was achieved. This made unbiased comparison between detector models performance possible and ensured reliability in the conclusions drawn from this study.

2.1.3 Calibration Goals

The calibration procedure aims to accurately set parameters related to four aspects of the reconstruction, which are:

1. **Digitisation of calorimeter hits.** Digitisation in this sense is the estimation of the energy deposited within a calorimeter cell, the active and absorber layers, based on the signal measured in the sensitive region of the cell, the active layer.
2. **Minimum ionising particle (MIP) scale setting in the digitisation processor and PandoraPFA.** The MIP scale has to be set in the digitiser as it simulates the response of the readout technology including a maximum readout value, which is in units of MIPs. The digitiser also applies a minimum active layer cell energy threshold, in units of MIPs, that has to be passed for creation of a calorimeter hit to occur. This is designed to veto noise that would be present in a real detector. PandoraPFA uses the MIP scale to place further threshold cuts on the cell energy that must be exceeded before a calorimeter cell is used in the reconstruction. Both of these thresholds are designed to veto noise that would be present in a real detector. While no noise is applied to the simulation these cuts are still applied to better represent the performance of a real detector.
3. **Electromagnetic and hadronic scale setting in PandoraPFA.** As discussed in chapter CALORIMETER CHAPTER, the response of a calorimeter to electromagnetic and hadronic showers is different due to the fundamentally different mechanisms governing their propagation. One key difference between the two is the presence of an invisible energy component in the hadronic shower. Therefore, the reported energy from a calorimeter to a hadronic showers will be lower than that of an electromagnetic shower. To account for effects such as this and to account for energy losses due to the application of noise vetoing cuts in PandoraPFA the PFO energies are rescaled by PandoraPFA depending on whether the PFO has showered electromagnetically or hadronically. Determination of these scaling factors is the setting of the electromagnetic and hadronic energy scales.
4. **Retraining photon likelihood data.** The PandoraPFA algorithm uses likelihood data to determine whether a reconstructed object is a photon. This likelihood data has to be retrained for every new detector model considered.

Each of these aspects needs separately addressing for each new detector model considered. The ordering of each of these calibration steps also had to be taken into

consideration as it is possible to get interference between the different stages if applied in the wrong order.

2.1.4 Digitisation

Calibration of the digitisation of the calorimeter hits involves accurately estimating the energy deposited in a calorimeter cell, in both the active and absorber layers, based on the energy deposited in the sensitive element of the calorimeter, the active layer. The relationship between the energy deposited in the active layers and the absorber layers of a calorimeter is linear as the energy deposited in both layers are proportional to the number of charged tracks passing through them. The ratio of the calorimeter cell energy to the energy deposited in the active layers is hereby called the digitisation constant. . The digitisation constants depend upon several aspects of the detector including the material properties of the calorimeters, the magnetic field strength and energy losses occurring within the gaps between the active and absorber layers. To account the effect of instrumented read out technology that would exist in a completed calorimeter some material is included in the simulation around the active and absorber layer. In comparison to the absorber layer this extra material adds little to the detector, but energy losses here are accounted for in digitisation.

ECal Digitisation

The procedure for determining the digitisation constants in the ECal involved the simulation of single γ events at $E_{MC} = 10$ GeV. γ events are ideal for calibration of the ECal as in the particle flow paradigm γ energy measurements are made primarily within the ECal. Also at this energy γ s are largely contained within the ECal, as shown in figure 2.1, making them ideal for isolating the ECal digitisation calibration from that of the HCal digitisation calibration.

Events are only considered in this analysis if they are confined to the ECal and to that extent cuts are applied ensuring that the sum of any reconstructed energy found outside the ECal is less than 1% of E_{MC} and that the $\cos(\theta) < 0.95$ where θ is the polar angle of the γ . γ conversions are also vetoed from this event sample at this stage by requiring the reconstruction to give a single photon PFO. The impact of these cuts on the sum of ECal calorimeter hit energies for the $E_{MC} = 10$ GeV γ events is shown in figure 2.2.

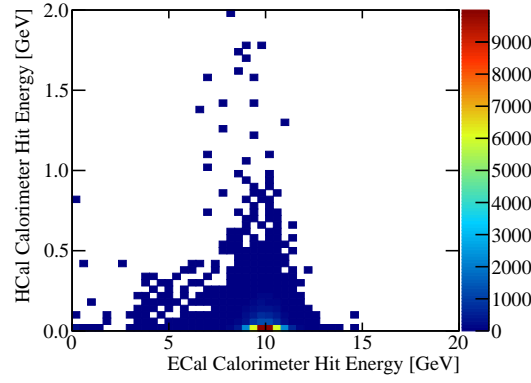


Figure 2.1: Sum of calorimeter hit energies in ECal and HCal for 10 GeV γ events.

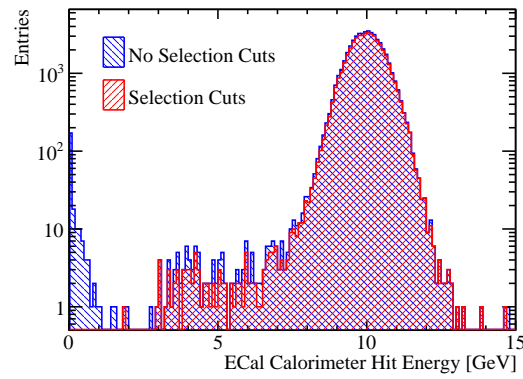


Figure 2.2: Sum of the ECal calorimeter hit energies for 10 GeV γ events with and without the selection cuts.

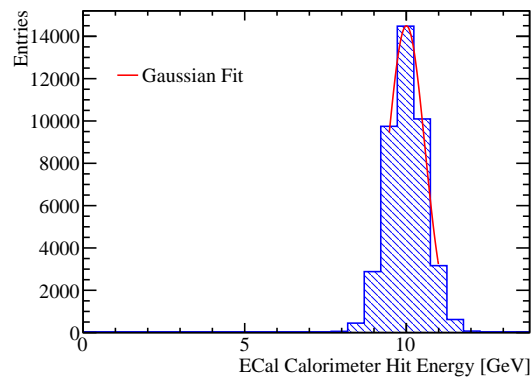


Figure 2.3: Gaussian fit to sum of the ECal calorimeter hit energies for 10 GeV γ events with selection cuts.

The calibration procedure is iterative and begins with the simulated single γ events using a trial calibration, with digitisation constant in the ECal α_{ECal}^0 , which may not be ideal. Then the distribution of the sum of calorimeter hit energies within the ECal is produced for events passing the selection cuts using, as shown in figure 2.2. For an ideal calorimeter this distribution should be Gaussian, as was described in section CALORIMETER CHAPTER. Therefore, a Gaussian fit is applied to this distribution and the mean, E_{Fit} , extracted. In an attempt to remove the effect of any outliers in this distribution, the fit is applied to the range of data with the smallest root mean square that contains at least 90 % of the data. An example of such a fit is shown in figure ???. In the case of perfect calibration the mean of this fit would be equal E_{MC} and it is assumed that any deviation between the two is due to inaccurate calibration. To correct for any such deviation the digitisation constant from the trial calibration, α_{ECal}^0 , is rescaled by the ratio of the E_{MC} to E_{Fit} .

$$\alpha_{\text{ECal}}^0 \rightarrow \alpha_{\text{ECal}} = \alpha_{\text{ECal}}^0 \times \frac{E_{\text{MC}}}{E_{\text{Fit}}} \quad (2.1)$$

This procedure is then repeated until the E_{Fit} falls within a chosen tolerance of E_{MC} . The tolerance that was applied here is that $|E_{\text{Fit}} - E_{\text{MC}}| < E_{\text{MC}} \times 5\%$. The binning for the fitted histogram is chosen such that the bin width is equal to the desired tolerance on E_{Fit} e.g. $E_{\text{MC}} \times 5\% = 0.5 \text{ GeV}$. This tolerance is somewhat large, however, it is tight enough to ensure successful application of PFA. It should also be emphasised that the PFO energies used in downstream analyses have the electromagnetic and hadronic energy scale corrections applied and these are calibrated to a much tighter accuracy.

HCal Digitisation

The calibration for the digitisation in the HCal proceeds in a similar manor to that described for the ECal with a few key differences. This calibration uses K_L^0 events at $E_{\text{MC}} = 20 \text{ GeV}$ as these neutral hadrons will deposit the bulk of their energy in the HCal. The higher energy is used to create larger particle showers and sample deeper into the calorimeters.

As the K_L^0 samples have to pass through the ECal before arriving at the HCal and as the ECal contains $\approx 1\lambda_I$, some of the particles begin showering in the ECal, as shown

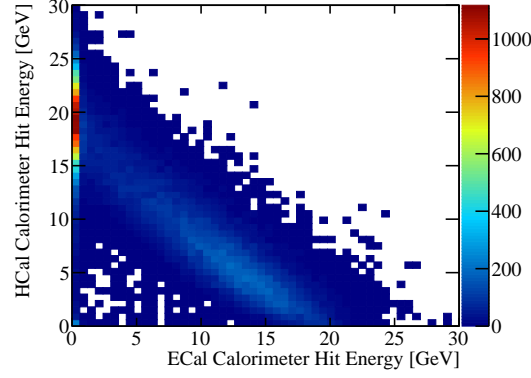


Figure 2.4: Sum of calorimeter hit energies in ECal and HCal for 20 GeV K_L^0 events.

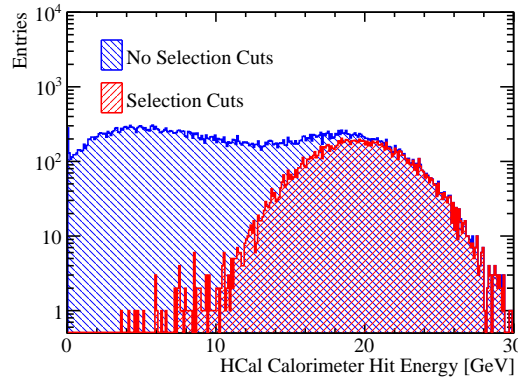


Figure 2.5: Sum of the HCal calorimeter hit energies for a 20 GeV K_L^0 events with and without the selection cuts.

by figure 2.4. These events are unsuitable for calibration as rescaling α_{HCal}^0 does not lead to a linear rescaling in the mean of E_{Fit} . This issue is resolved by applying selection cuts to select events that deposit the bulk of their energy in the HCal.

Events are only considered in this analysis if a single neutral hadron PFO is reconstructed, the sum of any reconstructed energy found outside the HCal is less than 5% of E_{MC} and the last layer of the HCal where energy is deposited is in the first 90% of the HCal. The cut on the last HCal layer where energy is deposited is applied to veto events that shower late in the HCal and deposit a significant amount of energy in the uninstrumented coil region of the detector. The impact of these cuts on the sum of HCal calorimeter hit energies for the $E_{\text{MC}} = 20$ GeV K_L^0 events is shown in figure 2.5.

There are two HCal digitisation constants used in the detector simulation, one applied for the HCal barrel and another for the HCal EndCap. This is to account for

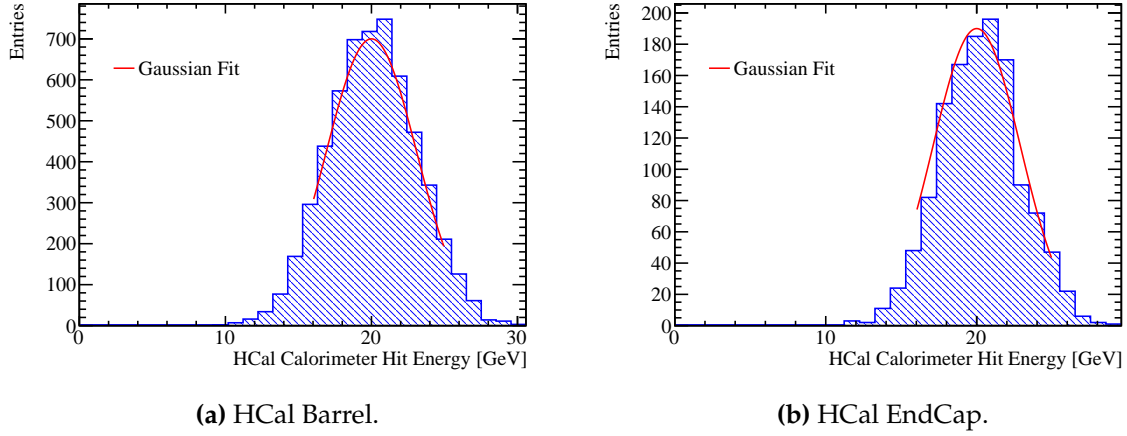


Figure 2.6: Gaussian fit to sum of the HCal calorimeter hit energies for 20 GeV K_L^0 events with selection cuts.

differences in hadronic shower dynamics that exist due to a variety of reasons such as differing magnetic field configurations in the Barrel and EndCap. Both parameters are calibrated in the same manor, but have different cuts on θ , the polar angle of the K_L^0 . For the Barrel region of the HCal $0.2 < \cos(\theta) < 0.6$, while for the EndCap $0.8 < \cos(\theta) < 0.9$. These angular cuts are conservative to account for the transverse profile of the hadronic showers and ensure that they are confined to the relevant sub-detector.

Using these cuts the calibration procedure for the digitisation of the HCal Barrel and EndCap proceeds in the same manor as was described for the ECal, the details of which can be found in section 2.1.4, and examples of the Gaussian fits applied to the sum of the calorimeter hit energies in the HCal Barrel and EndCap can be found in figure 2.6.

HCal Ring Digitisation

The HCal ring also has an independent digitisation constant for the same reasons that the Barrel and EndCap constants differ. The procedure used to calibrate this constant has to differ from that presented in section 2.1.4 as it is unfeasible, due to the depth of the ring, to produce events that are wholly contained within it. Fortunately, the size of the HCal ring means that it will play a minimal role in the reconstruction, so precise calibration is not crucial. To ensure that the calibration is approximately correct for the

HCal Ring, $\alpha_{\text{HCal Ring}}$ is assumed to equal $\alpha_{\text{HCal EndCap}}$ multiplied by several factors designed to accounts for changes in the active layer thickness, absorber layer thickness and the MIP response between the HCal EndCap and Ring. In detail:

$$\alpha_{\text{HCal Ring}} = \alpha_{\text{HCal EndCap}} \times \frac{\langle \cos(\theta_{\text{EndCap}}) \rangle}{\langle \cos(\theta_{\text{Ring}}) \rangle} \times \frac{P_{\text{EndCap}}}{P_{\text{Ring}}} \times \frac{L_{\text{EndCap}}^{\text{Absorber}}}{L_{\text{Ring}}^{\text{Absorber}}} \times \frac{L_{\text{Ring}}^{\text{Active}}}{L_{\text{EndCap}}^{\text{Active}}} \quad (2.2)$$

where θ is the incident angle of the incoming particle to the calorimeter cells determined using the 20 GeV K_L^0 events, L^{Active} is the active layer thickness, L^{Absorber} is the absorber layer thickness and P is the position of the MIP peak in the distribution of active layer cell energies, corrected so that the particles appear normally incident, using 10 GeV μ^- events. Details on how P is determined can be found in section 2.1.5.

2.1.5 MIP Scale Setting

The response of the various sub-detectors to a MIP has to be determined for both the digitisation processor and for PandoraPFA as both apply cuts in units of MIP response. The digitiser applies cuts related to the electronic readout range of the various active layer technology options and applies thresholds on the minimum active layer energy for the creation of calorimeter hits, while PandoraPFA applies cuts that would veto noise that would be present in a real detector. Both these MIP responses, while intrinsically linked, have to be calculated separately as the digitiser requires the MIP peak definition from the active layer cell energies while, PandoraPFA requires the definition from the full cell, active and absorber layer, energies. In these studies a MIP was defined as a 10 GeV μ^- [3] and there were no selection cuts applied to this sample.

For the digitiser the MIP scale was defined as the, non-zero, peak in the distribution of the active layer calorimeter cell energies for normally incident μ^- as shown in figure 2.7. This distribution was produced using a sample of μ^- events that are spatially isotropic about the impact point. A direction correction factor, $\cos(\theta)$ where θ is the indecent angle of the incoming μ^- to the calorimeter cell, was applied to the active layer cell energies to generate the effect of having normally incident μ^- .

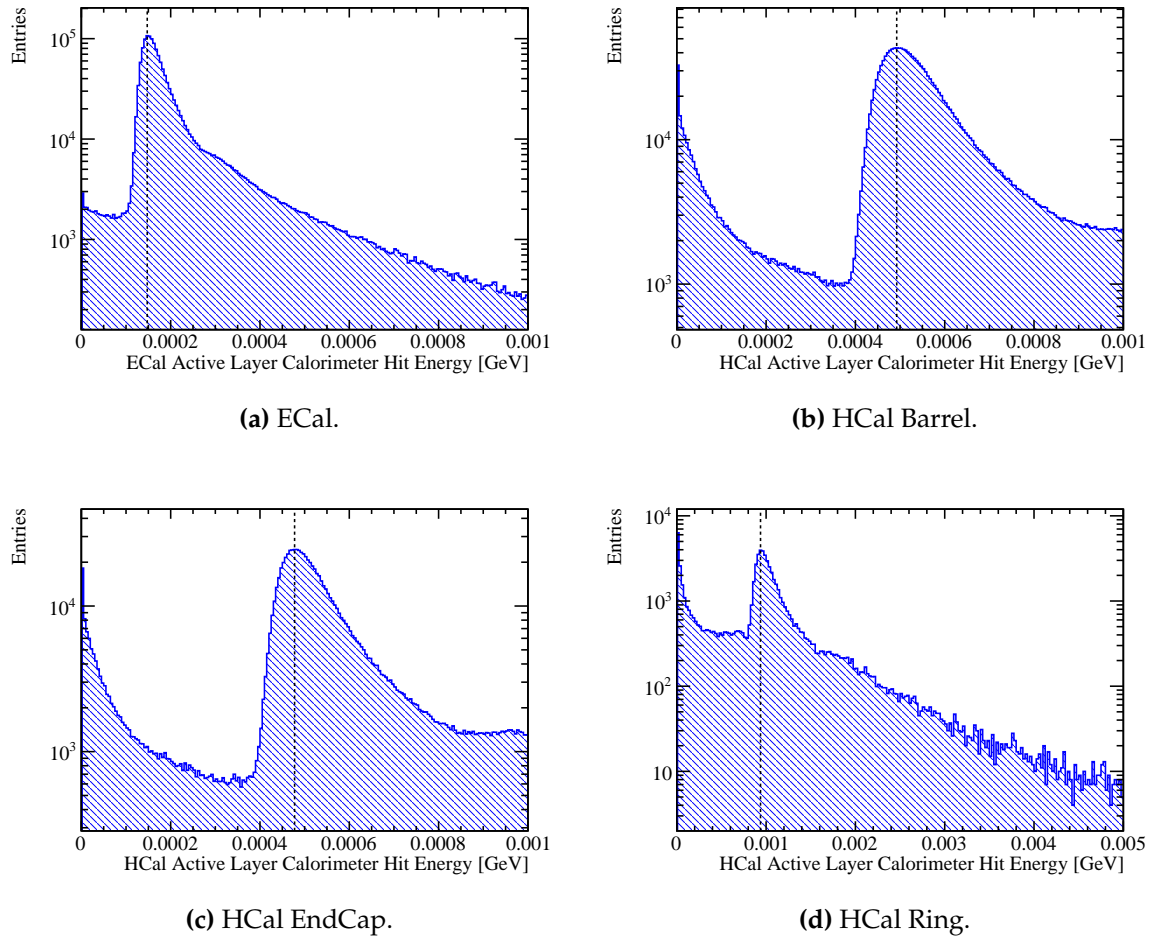


Figure 2.7: The active layer calorimeter cell energy distributions for various sub-detectors for 10 GeV μ^- events. The MIP peak is represented by the black dotted line.

In the digitiser processor a single value for the MIP peak was required for the HCal and that was taken as the MIP peak position for the HCal Barrel. The MIP peaks were separately calculated for the HCal EndCap and Ring for the purposes of the HCal Ring digitisation described in section 2.1.4. The realistic digitisation features present in the simulation of the ECal and HCal were not present for the muon chamber digitisation and so no MIP peak setting for that digitisation stage was required.

A similar procedure was employed for calculation of the MIP peak in PandoraPFA. One important difference was the distribution used for setting the MIP scale in PandoraPFA is the distribution of calorimeter cell energies, i.e. the energy in the active and absorber layers of a cell, and not just the active layer energies. Examples of the distributions used to set the MIP scale in PandoraPFA can be found in figure 2.8. There are few populated low calorimeter cell energy bins due to cuts applied in the digitiser on the minimum active layer energy required to make a calorimeter hit. The double peak structure in the ECal calorimeter hit energy distribution is present due to the doubling of the thickness of the ECal absorber material, from 2.1 mm to 4.2 mm tungsten, in the ILD detector model, which occurs for the back the first 10 layers of the 30 layer ECal. Two differences between the MIP scale setting in the digitiser and PandoraPFA worthy of note are that for the PandoraPFA MIP scale setting the HCal sub-detectors, the Barrel, EndCal and Ring, are all combined into a single cell energy distribution and PandoraPFA requires the MIP scale to be set in the muon chamber, which required a muon chamber cell energy distribution to be created.

2.1.6 Electromagnetic and hadronic scale setting

The electromagnetic and hadronic scales have to be independently set in the simulation to account for the different mechanisms governing the propagation of electromagnetic and hadronic showers. As referenced earlier, one crucial difference the setting of these scales accounts for is the invisible energy component of hadronic showers, however, in this simulation it also accounts for the effect of energy loss due to the threshold cuts that are applied in the reconstruction. The setting of the scales involves tuning four parameters in PandoraPFA, which correspond to the scaling factors that are applied to PFO energies arising from electromagnetic and hadronic showering particles in the ECal and HCal.

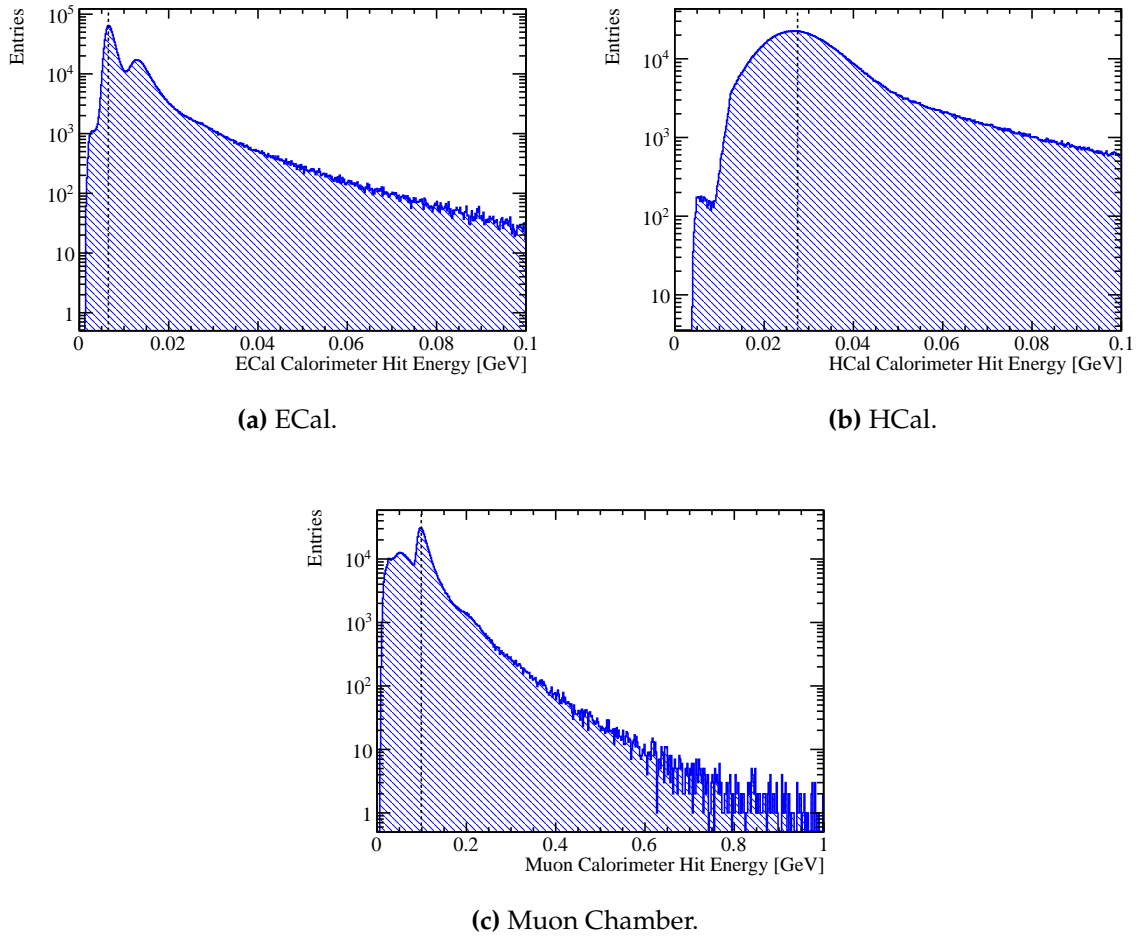


Figure 2.8: The calorimeter cell energy distributions for various sub-detectors for 10 GeV μ^- events. The MIP peak is represented by the black dotted line.

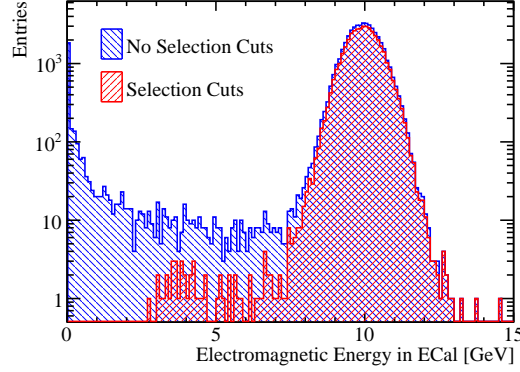


Figure 2.9: Sum of the electromagnetic energy measured in the ECal for 10 GeV γ events with and without the selection cuts.

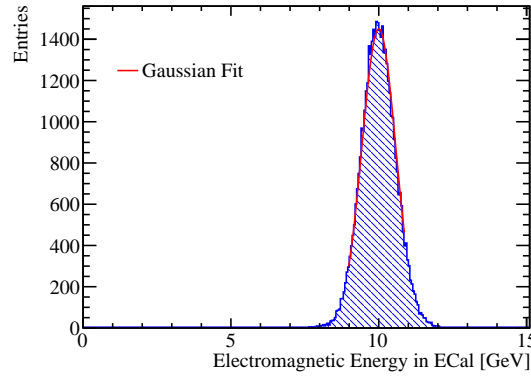


Figure 2.10: Gaussian fit to sum of the electromagnetic energy deposited in the ECal for 10 GeV γ events with selection cuts.

Electromagnetic scale setting

The electromagnetic scale in the ECal, β_{ECal}^{EM} , is set in the detector using γ events at $E_{MC} = 10$ GeV. γ events are ideal for the setting of the electromagnetic scale as they produce electromagnetic showers and are primarily confined to the ECal at the energy considered as was shown in figure 2.1.

Cuts are applied to ensure that only events where the bulk of the energy is deposited within the ECal are applied. The cuts require a single γ be reconstructed, excluding conversions, and that less than 1% of the reconstructed energy is outside the ECal. The impact of these cuts on the electromagnetic energy measured in the ECal for these 10 GeV γ events is shown in figure 2.9.

The fitting procedure proceeds in a similar manor to that described in section 2.1.4 whereby a trial calibration for the electromagnetic energy scale in the ECal, β_{ECal}^{EM0} , is assumed and the single γ events simulated. The distribution of the PFO electromagnetic energy in the ECal is produced and a Gaussian fit applied to the range of data with the smallest root mean square that contains at least 90 % of the data. The mean of this fit, E_{Fit} , is then used to scale β_{ECal}^{EM0} in the following way

$$\beta_{ECal}^{EM0} \rightarrow \beta_{ECal}^{EM} = \beta_{ECal}^{EM0} \times \frac{E_{MC}}{E_{Fit}} \quad (2.3)$$

An example distribution and fit used for calibration of the nominal ILD detector model can be found in figure 2.10. The procedure is then repeated using the updated β_{ECal}^{EM} until E_{Fit} falls within a chosen tolerance, which in this case is that $|E_{Fit} - E_{MC}| < E_{MC} \times 0.5\%$. The binning for the fitted histogram is chosen such that the bin width is equal to the desired tolerance on E_{Fit} e.g. $E_{MC} \times 0.5\% = 0.05$ GeV. This tolerance is tighter than that applied for the digitisation as it is the PFO energies that are used in downstream analyses and therefore require high precision.

The electromagnetic scale in the HCal, β_{HCal}^{EM} , is chosen to be equal to the hadronic scale in the HCal, β_{HCal}^{Had} . The details of the determination of β_{HCal}^{Had} can be found in section 2.1.6. For ILC like energies, β_{HCal}^{EM} is not a critical parameter in the reconstruction as photons are largely contained within the ECal meaning little to no electromagnetic energy is measured in the HCal.

Hadronic scale setting

β_{ECal}^{Had} is important to detector performance as a non-negligible amount of hadronic energy is recorded in the ECal. However, as the ECal contains $\approx 1\lambda_I$, the hadronic scale in the ECal cannot be independently as it is unfeasible to create a large sample of 20 GeV K_L^0 events that are fully contained within it. Therefore, the hadronic scale is set in the ECal and HCal simultaneously.

Cuts applied to select K_L^0 that are appropriate to use for the hadronic scale calibration. The last layer in which energy is deposited in the HCal must not occur in the back 10 % of the HCal to ensure the event will not suffer from leakage. A single neutral hadron must be reconstructed to veto events with reconstruction failures. Finally, the

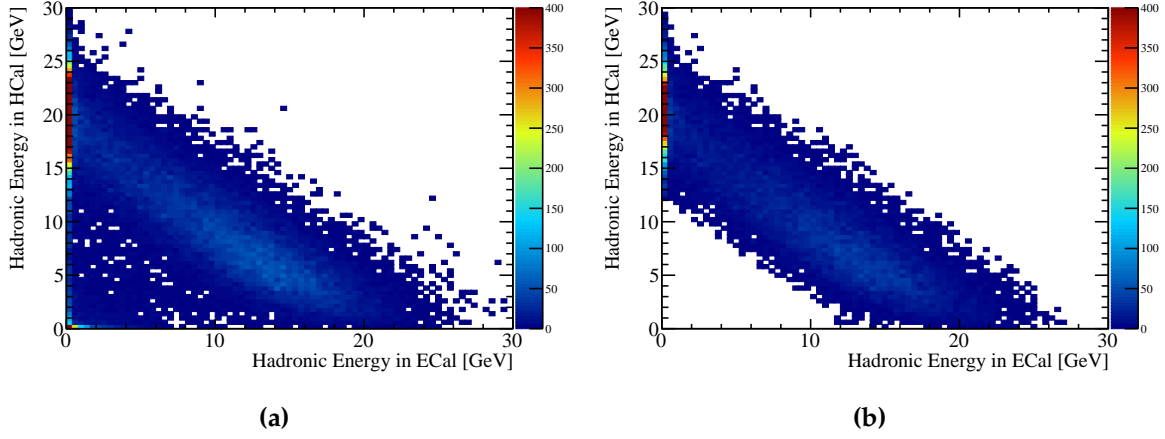


Figure 2.11: The distribution of hadronic energy measured in the ECal and HCal for 20 GeV K_L^0 events (a) without selection cuts and (b) with selection cuts.

total hadronic energy measured in ECal and HCal, $E_{ECal}^{Had} + E_{HCal}^{Had}$, must fall within 3σ of the desired hadronic energy distribution, $E_{ECal}^{Had} + E_{HCal}^{Had} = 20\text{GeV} - m_{K_L^0} = E_{MC}$. σ is defined to be $55\% \times \sqrt{E} = 2.46\text{GeV}$ for 20 GeV K_L^0 . This definition of sigma is the nominal energy resolution for neutral hadrons in the ILD HCal. This cut ensures that when fitting the two dimensional distribution of hadronic energy measured in the ECal and HCal the outliers do not skew the fit. These cuts are illustrated in in figure 2.11.

The calibration procedure is iterative and begins by assuming trial values, β_{ECal}^{Had0} and β_{HCal}^{Had0} , for the hadronic scale calibration factors β_{ECal}^{Had} and β_{HCal}^{Had} . The 20 GeV K_L^0 events are then simulated and reconstructed. Following this a linear fit to the distribution of E_{ECal}^{Had} against E_{HCal}^{Had} for 20 GeV K_L^0 events passing the selection cuts is applied. The fit is performed by minimising χ^2 , which is defined as

$$\chi^2(\delta_{ECal}^{Had}, \delta_{HCal}^{Had}) = \sum_i \frac{x_i}{\sigma_{x_i}} \quad (2.4)$$

where x_i is the perpendicular distance from E_{ECal}^{Had} and E_{HCal}^{Had} for event i to the line $E_{HCal}^{Had} = \delta_{HCal}^{Had} - E_{ECal}^{Had} \frac{\delta_{HCal}^{Had}}{\delta_{ECal}^{Had}}$. The definition of x_i is given in equation 2.5, but best illustrated by considering figure 2.12. σ_{x_i} is the uncertainty on x_i , which is calculated by propagating the uncertainties on E_{ECal}^{Had} and E_{HCal}^{Had} , which are assumed to

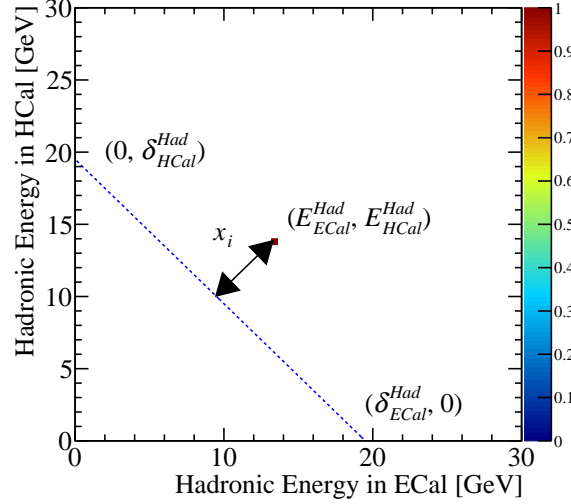


Figure 2.12: An example showing the definition of x_i , the variable used for the calculation of χ^2 for the setting of the hadronic energy scale. For an event that has been measured with hadronic energy E_{ECal}^{Had} in the ECal and E_{HCal}^{Had} in the HCal, the geometric interpretation of x_i is shown. The blue dotted line is defined as $E_{HCal}^{Had} = \delta_{HCal}^{Had} - E_{ECal}^{Had} \frac{\delta_{HCal}^{Had}}{\delta_{ECal}^{Had}}$.

be $\sigma_{E_{E/HCal}^{Had}} = 55\% \times \sqrt{E_{E/HCal}^{Had}}$, into the expression for x_i . The result of this propagation of errors is given in equation 2.6. The sum runs over all events, i , passing the selection cuts.

$$x_i = \frac{E_{HCal}^{Had} \delta_{ECal}^{Had} + E_{ECal}^{Had} \delta_{HCal}^{Had} - \delta_{ECal}^{Had} \delta_{HCal}^{Had}}{\sqrt{(\delta_{ECal}^{Had})^2 + (\delta_{HCal}^{Had})^2}} \quad (2.5)$$

$$\sigma_i = \frac{(\sigma_{E_{HCal}^{Had}} \delta_{ECal}^{Had})^2 + (\sigma_{E_{ECal}^{Had}} \delta_{HCal}^{Had})^2}{\sqrt{(\delta_{ECal}^{Had})^2 + (\delta_{HCal}^{Had})^2}} \quad (2.6)$$

The minimisation steps across a range of δ_{ECal}^{Had} and δ_{HCal}^{Had} centred about the ideal value of $20 \text{ GeV} - m_{K_L^0}$ in search for the minimum χ^2 . Once the minima in χ^2 is found the trial calibration factors β_{ECal}^{Had0} and β_{HCal}^{Had0} are rescaled to correct for any deviation from the desired fit as follows

$$\beta_{ECal}^{Had0} \rightarrow \beta_{ECal}^{Had} = \beta_{ECal}^{Had0} \times \frac{E_{MC}}{\Delta_{ECal}^{Had}} \quad (2.7)$$

$$\beta_{HCal}^{Had0} \rightarrow \beta_{HCal}^{Had} = \beta_{HCal}^{Had0} \times \frac{E_{MC}}{\Delta_{HCal}^{Had}} \quad (2.8)$$

where Δ_{ECal}^{Had} and Δ_{HCal}^{Had} are the values of δ_{ECal}^{Had} and δ_{HCal}^{Had} giving the minimum χ^2 . The step sizes used for minimising χ^2 with respect to δ_{ECal}^{Had} and δ_{HCal}^{Had} is chosen such that a single step corresponds to the target final tolerance on δ^{Had} i.e. $|\delta_{E/HCal}^{Had} - E_{MC}| < E_{MC} \times 0.5\% \approx 0.1\text{GeV}$.

This procedure is then repeated until Δ_{ECal}^{Had} and Δ_{HCal}^{Had} both fall within a given tolerance, which in this case it taken to be $|\Delta_{E/HCal}^{Had} - E_{MC}| < E_{MC} \times 0.5\% \approx 0.1\text{GeV}$

Colophon

This thesis was made in $\text{\LaTeX}2_\epsilon$ using the “hepthesis” class [\[4\]](#).

Bibliography

- [1] S. Agostinelli et al. GEANT4: A Simulation toolkit. *Nucl. Instrum. Meth.*, A506:250–303, 2003.
- [2] G. Alexander et al. A Comparison of b and (uds) quark jets to gluon jets. *Z. Phys.*, C69:543–560, 1996.
- [3] H. Bichsel, Donald E. Groom, and S. R. Klein. Passage of particles through matter. 2004.
- [4] Andy Buckley. The hepthesis L^AT_EX class.
- [5] F. Gaede. Marlin and LCCD: Software tools for the ILC. *Nucl. Instrum. Meth.*, A559:177–180, 2006.
- [6] J. S. Marshall, A. M \ddot{a} ijnnich, and M. A. Thomson. Performance of Particle Flow Calorimetry at CLIC. *Nucl. Instrum. Meth.*, A700:153–162, 2013, 1209.4039.
- [7] P. Mora de Freitas and H. Videau. Detector simulation with MOKKA / GEANT4: Present and future. In *Linear colliders. Proceedings, International Workshop on physics and experiments with future electron-positron linear colliders, LCWS 2002, Seogwipo, Jeju Island, Korea, August 26-30, 2002*, pages 623–627, 2002.
- [8] C. Patrignani et al. Review of Particle Physics. *Chin. Phys.*, C40(10):100001, 2016.
- [9] Torbjorn Sjostrand, Stephen Mrenna, and Peter Z. Skands. PYTHIA 6.4 Physics and Manual. *JHEP*, 05:026, 2006, hep-ph/0603175.
- [10] M. A. Thomson. Particle Flow Calorimetry and the PandoraPFA Algorithm. *Nucl. Instrum. Meth.*, A611:25–40, 2009, 0907.3577.

List of figures

1.1	500 GeV di-jet $Z \rightarrow uds$ event display for nominal ILD detector.	2
1.2	Definition of jet energy resolution. Reconstructed jet energy for 200 GeV di-jet $Z \rightarrow uds$ events for nominal ILD detector.	3
1.3	Reconstructed energy distribution using nominal ILD detector model.	5
1.4	Jet energy resolution as a function of jet energy for the nominal ILD detector.	7
1.5	Energy resolution as a function of photon energy for the nominal ILD detector for both the silicon and scintillator options.	8
1.6	Energy resolution as a function of K_L^0 energy for the nominal ILD detector.	8
1.7	Jet energy resolution as a function of ECal cell size.	10
1.8	Jet energy resolution breakdown as a function of ECal transverse granularity for 45 and 250 GeV jets. Results are given for both the silicon and scintillator ECal options.	11
1.9	Energy resolution as a function of ECal transverse granularity for 100 GeV photons. Results are given for both the silicon and scintillator ECal options.	11
1.10	Jet energy resolution as a function of longitudinal granularity in the ECal.	13
1.11	Jet energy resolution breakdown as a function of ECal longitudinal granularity for 45 and 250 GeV jets. Results are given for both the silicon and scintillator ECal options.	14

1.12 Energy resolution as a function of ECal longitudinal granularity for 100 GeV photons. Results are given for both the silicon and scintillator ECal options.	15
1.13 Jet energy resolution as a function of jet energy for various absorber materials in the HCal and physics lists.	18
1.14 Jet energy resolution breakdown as a function of HCal absorber material and physics list for 45 and 250 GeV jets.	18
1.15 Jet energy resolution as a function of HCal cell size.	19
1.16 Jet energy resolution breakdown as a function of HCal transverse granularity for 45 and 250 GeV jets.	20
1.17 Energy resolution as a function of HCal transverse granularity for 50 GeV K_L^0	20
1.18 Jet energy resolution as a function of number of layers in the HCal. . .	21
1.19 Jet energy resolution breakdown as a function of number of layers in the HCal for 45 and 250 GeV jets.	22
1.20 Energy resolution as a function of number of layers in the HCal for 50 GeV K_L^0	22
1.21 Jet energy resolution as a function of sampling frequency in the HCal. . .	24
1.22 Jet energy resolution as a function of sampling frequency in the HCal. . .	25
1.23 Jet energy resolution breakdown as a function of HCal sampling frequency for 45 and 250 GeV jets.	25
1.24 Energy resolution as a function of HCal sampling frequency for 50 GeV K_L^0	26
1.25 Jet energy resolution as a function of magnetic field strength.	27
1.26 Jet energy resolution breakdown as a function of magnetic field strength for 45 and 250 GeV jets.	28
1.27 Jet energy resolution as a function of ECal inner radius.	29

1.28	Jet energy resolution breakdown as a function of ECal inner radius for 45 and 250 GeV jets.	30
2.1	Sum of calorimeter hit energies in ECal and HCal for 10 GeV γ events.	35
2.2	Sum of the ECal calorimeter hit energies for 10 GeV γ events with and without the selection cuts.	35
2.3	Gaussian fit to sum of the ECal calorimeter hit energies for 10 GeV γ events with selection cuts.	35
2.4	Sum of calorimeter hit energies in ECal and HCal for 20 GeV K_L^0 events.	37
2.5	Sum of the HCal calorimeter hit energies for a 20 GeV K_L^0 events with and without the selection cuts.	37
2.6	Gaussian fit to sum of the HCal calorimeter hit energies for 20 GeV K_L^0 events with selection cuts.	38
2.7	The active layer calorimeter cell energy distributions for various sub-detectors for 10 GeV μ^- events.	40
2.8	The calorimeter cell energy distributions for various sub-detectors for 10 GeV μ^- events.	42
2.9	Sum of the electromagnetic energy measured in the ECal for 10 GeV γ events with and without the selection cuts.	43
2.10	Gaussian fit to sum of the electromagnetic energy deposited in the ECal for 10 GeV γ events with selection cuts.	43
2.11	The distribution of hadronic energy measured in the ECal and HCal for 20 GeV K_L^0 events with and without selection cuts.	45
2.12	An example showing the definition of x_i , the variable used for the calculation of $\chi^2(\delta_{ECal}^{Had}, \delta_{HCal}^{Had})$ for the setting of the hadronic energy scale.	46

List of tables

1.1	Nominal ILD detector model ECal configuration.	9
1.2	Transverse granularity layout of the ECal models considered.	12
1.3	Nominal ILD detector model HCal configuration.	16
1.4	Sampling fraction of HCal models considered.	23
1.5	Transverse granularity layout of various HCal models considered. . . .	24